Supplementary Information

SF2312 is a natural phosphonate inhibitor of Enolase

Paul G. Leonard*[1], Nikunj Satani*[2], David Maxwell[3], Yu-Hsi Lin[2], Naima Hammoudi[2], Zhenghong Peng[4], Federica Pisaneschi[2], Todd M. Link[1], Gilbert R. Lee[1], Duoli Sun, Basvoju A. Bhanu Prasad, Maria Emilia Di Francesco[1], Barbara Czako[1], John M. Asara[5], Y. Alan Wang[6], William Bornmann[7], Ronald A. DePinho[6] and Florian L. Muller[#2]

1) Institute for Applied Cancer Science, University of Texas MD Anderson Cancer Center, Houston, TX 77054
2) Department of Cancer Systems Imaging, University of Texas MD Anderson Cancer Center, Houston, TX 77054
3) Department of Clinical Analytics & Informatics, Houston, TX 77054-3403
4) Cardtronics, Inc., Houston, TX 77042
5) Department of Medicine, Beth Israel Deaconess Medical Center and Harvard Medical School, Boston, MA 02115
6) Department of Cancer Biology, University of Texas MD Anderson Cancer Center, Houston, TX 77030, USA University of Texas MD Anderson Cancer Center, Houston, TX 77054 USA
7) Bayou Therapeutics, Inc, Missouri City, TX 77459-3028

*) Co-first authors

#) To whom correspondence should be addressed: fmuller@mdanderson.org

Supplementary Results

Supplementary Table 1. IC50 of PhAH and SF2312 against ENO1 and ENO2.

Supplementary Table 2. Data collection and refinement statistics (molecular replacement)

Supplementary Figure 1. Modeling of Enolase inhibitors with human ENO2

Supplementary Figure 2. SF2312 is as slow binding inhibitor with a lower k_{off} for ENO2 than ENO1.

Supplementary Figure 3. Structural analogues of SF2312 as inhibitors of other Enolase superfamily members.

Supplementary Figure 4. SF2312 stabilizes Enolase1 against thermal denaturation.

Supplementary Figure 5. SF2312 has no effect on thermal denaturation on proteins other than Enolase.

Supplementary Figure 6. SF2312 stabilizes recombinant human Enolase2 against thermal denaturation.

Supplementary Figure 7. Expression of Enolase in ENO1-deleted, ENO1-rescued and ENO2-rescued glioma cells.

Supplementary Figure 8. Selective toxicity of PhAH to ENO1 deleted glioma cells.

Supplementary Figure 9. SF2312 selectively inhibits the proliferation of ENO1-deleted glioma cells.

Supplementary Figure 10. Toxicity of SF2312 against ENO1 deleted glioma cells is increased under hypoxia.

Supplementary Figure 11. SF2312 selectively depletes ATP in ENO1-deleted glioma cells.

Supplementary Figure 12. Effect of SF2312 and PhAH on cell death and cell number in ENO1-deleted and isogenic rescued glioma cells.

Supplementary Figure 13. SF2312 selectively inhibits glycolysis in ENO1-deleted glioma cells.

Supplementary Figure 14. SF2312 selectively inhibits conversion of uniformly labeled 13C-glucose to 13C-lactate in ENO1-deleted glioma cells.

Supplementary Figure 15. Effects of SF2312 on glycolytic intermediates immediately around the Enolase step raw data.

Supplementary Figure 16. Effects of SF2312 on glycolytic intermediates immediately around the Enolase step normalized.

Supplementary Figure 17. SF2312 treatment leads to a build-up of intermediates upstream of Enolase.

Supplementary Figure 18. Thermal stabilization of ENO2 by SF2312 and PhAH in intact glioma cells.

Supplementary Figure 19. ENO1-deleted glioma cells have profoundly decreased Enolase activity.

Supplementary Figure 20. Uncropped western blot scans for Figure 2.

Supplementary Figure 21. Uncropped western blot scans for Supplementary Figure 4.

Supplementary Figure 22. Uncropped western blot scans for Supplementary Figure 5.

Supplementary Figure 23. Uncropped western blot scans for Supplementary Figure 6.

Supplementary Figure 24. Uncropped western blot scans for Supplementary Figure 7.

Supplementary Figure 25. Uncropped western blot scans for Supplementary Figure 18.

Supplementary Figure 26. Uncropped western blot scans for Supplementary Figure 19a.

Supplementary Table 1. *IC_{50} of PhAH and SF2312 against ENO1 and ENO2.*

	PhaH (nM)	SF2312 (nM)
Recombinant hENO1	53.2	37.9
Recombinant hENO2	62.3	42.5
Mouse Liver	70.1 ± 23.3	22.1 ± 5.7
Mouse Brain	49.7 ± 3.5	13.8 ± 2.9
pCMV ENO1	21.0 ± 3.1	13.4 ± 2.0
pCMV ENO2	23.2 ± 6.5	14.4 ± 2.3

Enolase activity was measured as described in the methods, with the average IC_{50} ± S.E.M. in nM being shown. hENO1, hENO2 human recombinant Enolase (N = 2); pCMV ENO1, ENO2 human enolase expressed in cancer cell lines (N = 8), Mouse Liver, Brain: lysates from mouse brain and liver (N = 3).

Supplementary Table 2 Data collection and refinement statistics (molecular replacement)

	Enolase 2: PhaH (PDB 4ZA0)	Enolase 2:SF2312 (PDB 4ZCW)
Data collection		
Space group	P 2_1 2_1 2_1	P 2_1 2_1 2_1
Cell dimensions		
a, *b*, *c* (Å)	67.79, 108.67, 112.21	68.30, 109.46, 117.27
α, β, γ (°)	90.00, 90.00, 90.00	90.00, 90.00, 90.00
Resolution (Å)	67.8–2.31 (2.39– 2.31)*	80.0–1.99 (2.04–1.99)*
R_{merge}	0.220 (0.840)	0.092 (0.449)
$I / \sigma I$	10.9 (3.1)	13.3 (3.8)
Completeness (%)	100.0 (100.0)	100.0 (99.6)
Redundancy	12.4 (11.4)	7.0 (6.6)
Refinement		
Resolution (Å)	58.0-2.31	51.7-1.99
No. reflections	37211	60788
R_{work} / R_{free}	0.164 / 0.204	0.157 / 0.202
No. atoms		
Protein	6629	6685
Ligand/ion	22	28
Water	488	593
B-factors		
Protein	19.6	24.6
Ligand/ion	22.1	18.7
Water	25.3	32.5
R.m.s. deviations		
Bond lengths (Å)	0.009	0.018
Bond angles (°)	0.638	1.396

Each protein structure was determined using data collected on a single crystal. *Highest-resolution shell is shown in parentheses.

Supplementary Figure 1

A)

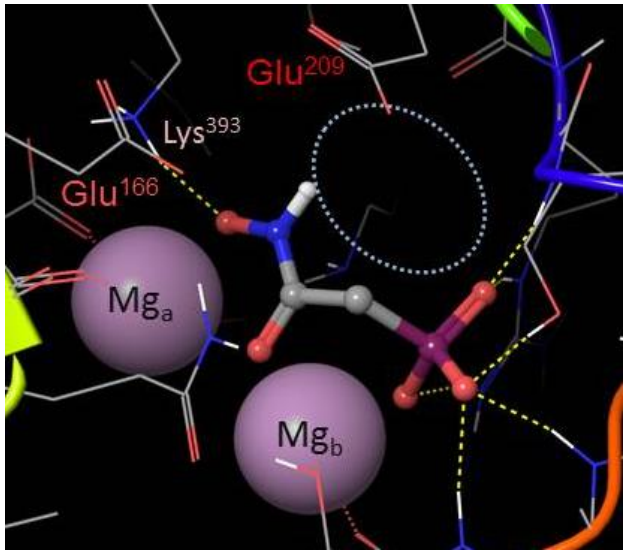

B)

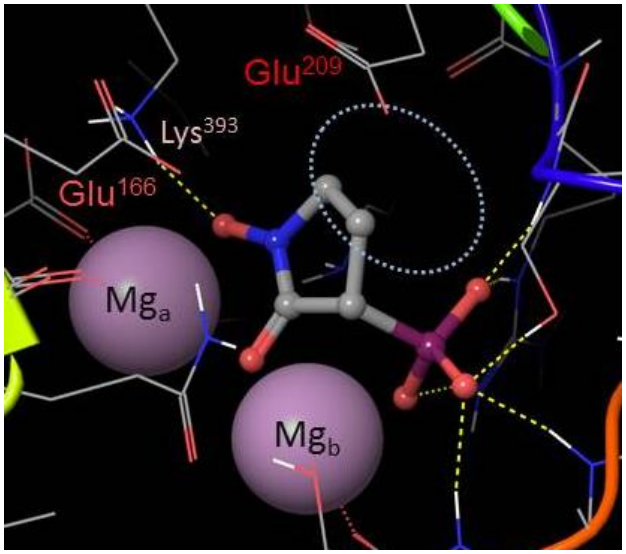

C)

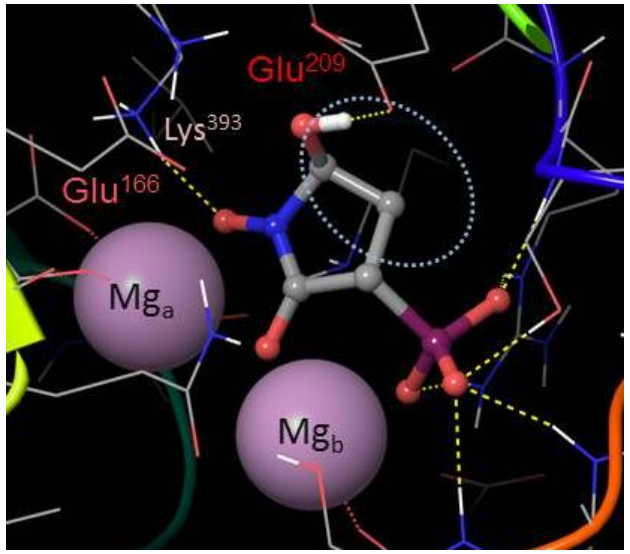

D)

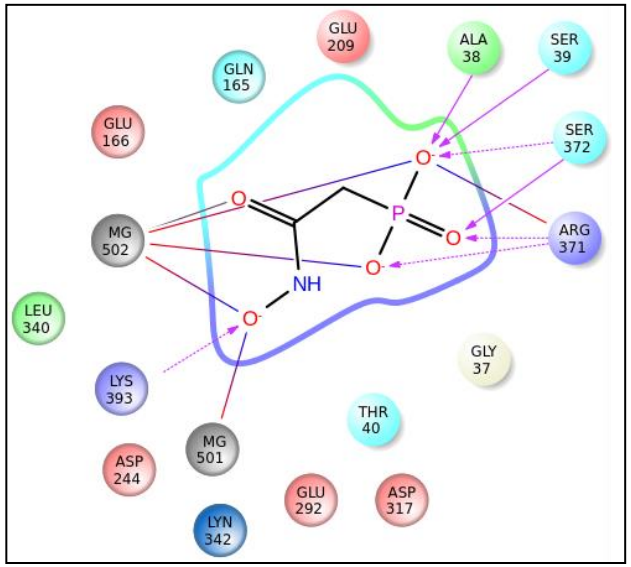

E)

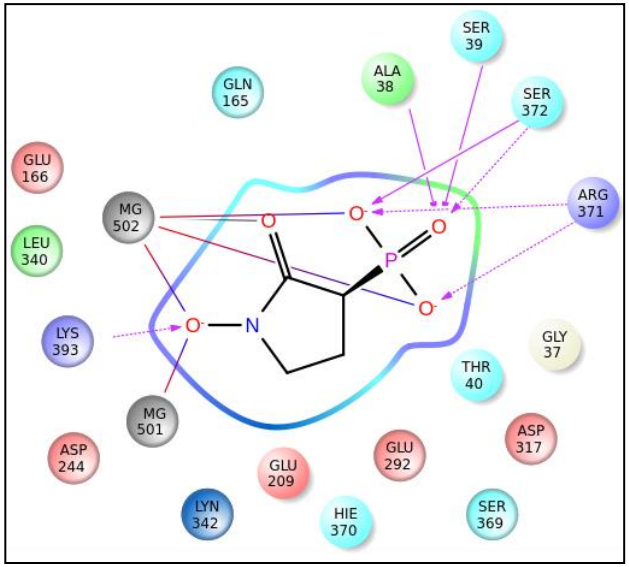

F)

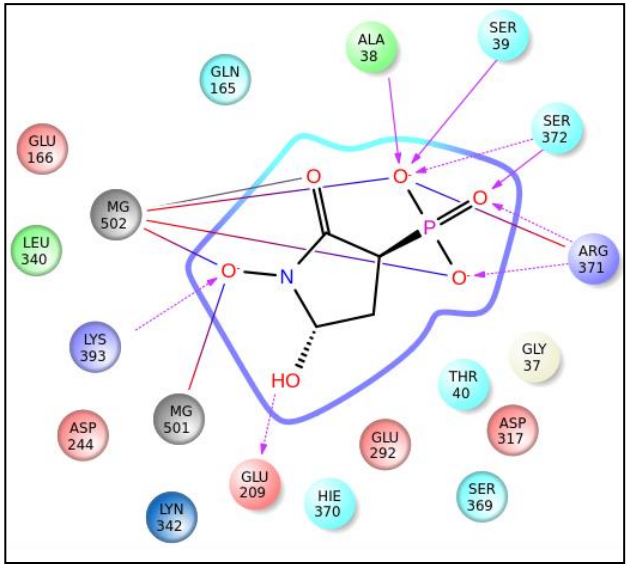

Supplementary Figure 1: *Modeling of Enolase inhibitors with human ENO2*

PhAH was docked into the structure of human ENO2 previously co-crystalized with the substrate PEP (PDB: 3UCD; **Panel A, D**). Docking of PhAH to ENO2 was modeled on the structures of PhAH bound to yeast and trypanosome enolase (1ELS, 2PTZ, 2PUO), where the inhibitor binds to the di-magnesium center with the carbonyl forming an oxo-bridge between the two Mg atoms (large spheres in light pink). The PhAH-docked structure revealed extensive unoccupied volume (dashed blue circle) in an otherwise highly spatially constrained active site. For the hypothesized, circular backbone stabilized molecules, the previously unoccupied space is now occupied by carbon atoms forming the circular backbone (**Panel B, E**) and in the case of SF2312 an additional hydroxyl-group that forms a hydrogen bond with one of the highly conserved catalytic glutamic acid residues (**Panel C, F**). Highly conserved residues required for catalytic function: Glu166, Glu209, Lys393 (hEnolase 2 numbering) are shown (40). Residues that are less than 4Å from the inhibitor are shown in cartoons with those forming direct interactions pointed out by lines (**Panels D, E**, **F**).

Supplementary Figure 2

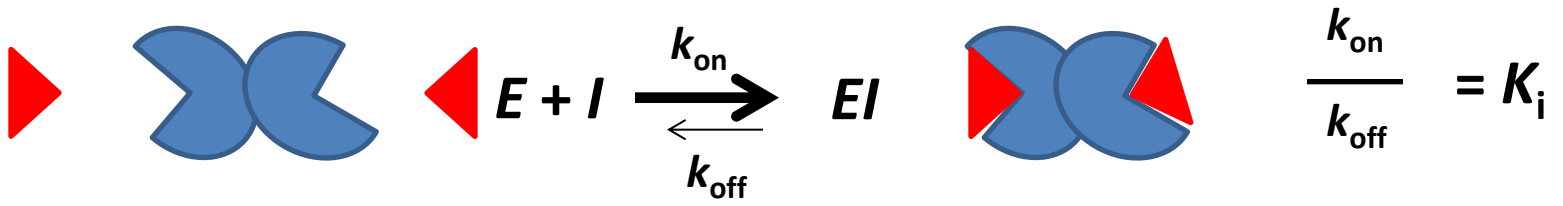

A)

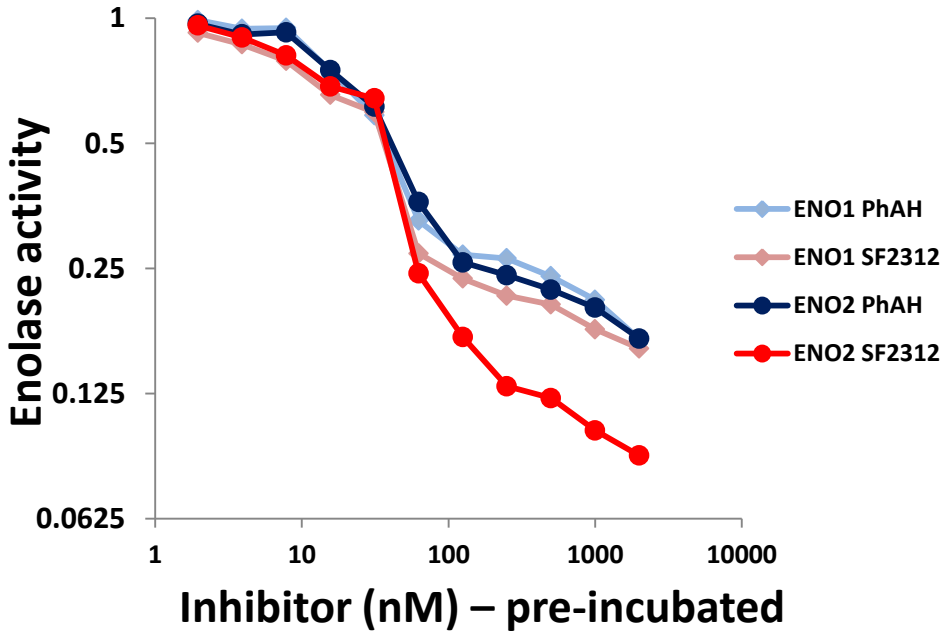

B)

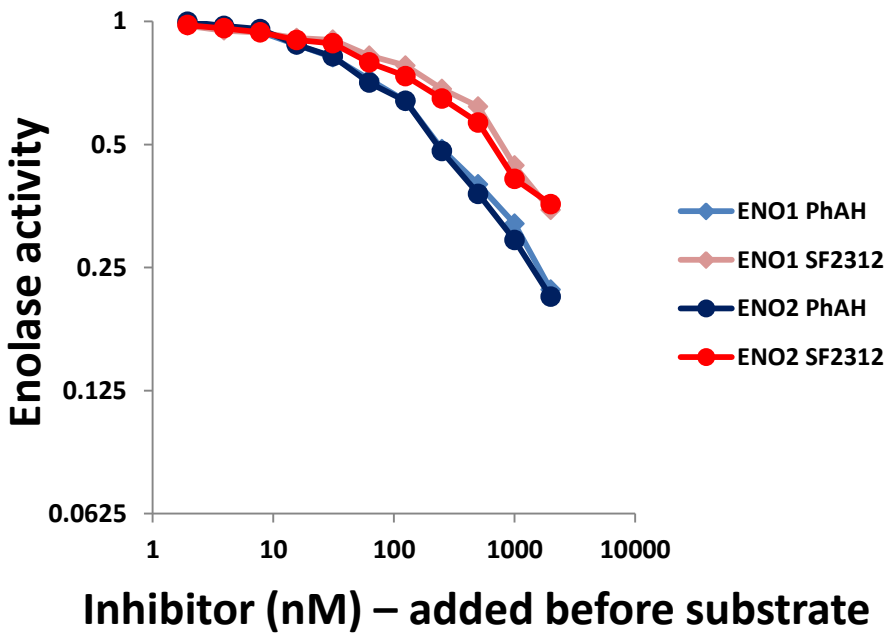

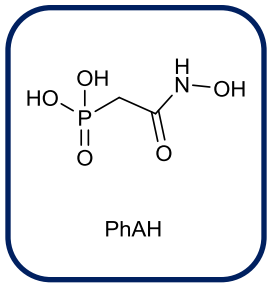

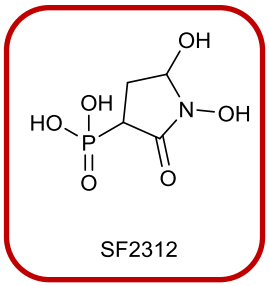

Supplementary Figure 2: *SF2312 is a slow binding inhibitor with a lower k_{off} for ENO2 than ENO1.* **Panel A)**: Pre-incubation of PhAH (blue/light blue, for ENO2 and ENO1, respectively) or SF2312 (red/crimson) as described in Figure 1 before the addition of the substrate 2-PGA resulted in profound inhibition of enzymatic activity (IC_{50} ~20 nM); inhibition of ENO2 with SF2312 was more profound and more durable than ENO1 (IC_{80} for SF2312 is 10 - fold lower for ENO2 than ENO1) while PhAH caused more or less equal inhibition of ENO1 and ENO2. **Panel B).** Addition of SF2312/PhAH prior to 2-PGA resulted in much weaker inhibition than if the inhibitors were pre-incubated before addition of substrate; this behavior was described previously for PhAH inhibition of yeast enolase, i.e. PhAH acts as a "slow" k_{on} inhibitor. SF2312 was actually less potent than PhAH when assayed under these conditions, indicating that it shows an even slower k_{on} than PhAH. Since SF2312 is more potent than PhAH when pre-incubated prior to addition of substrate, this indicates that SF2312 has a much slower k_{off} than PhAH and that the increased inhibitory potency of SF2312 against ENO2 over ENO1 is due to differences in k_{off} rather than k_{on}. SF2312, like PhAH, binds the di-Mg form of the enzyme. ENO2 has higher affinity of ENO2 for Mg_b may explain the slower k_{off} for SF2312 in ENO2 versus ENO1. The experiment was reproduced independently twice, a representative plot is shown

Supplementary Figure 3

PhAH

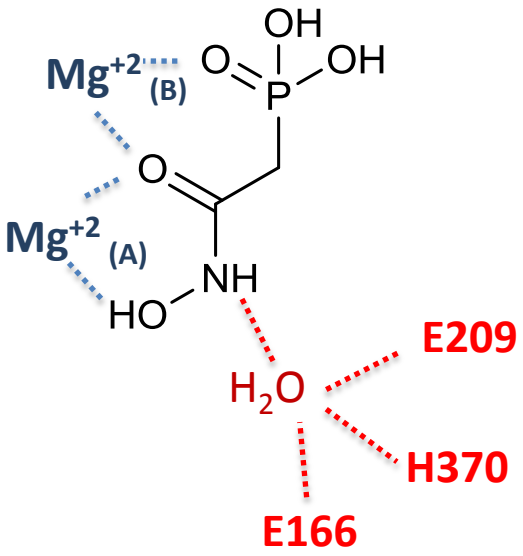

SF 2312

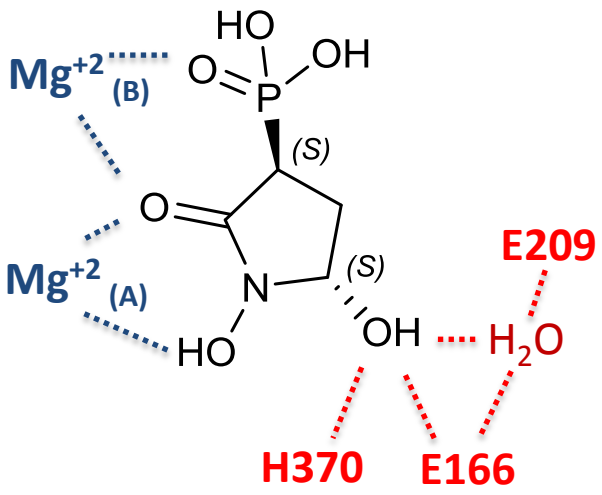

Alahopcin

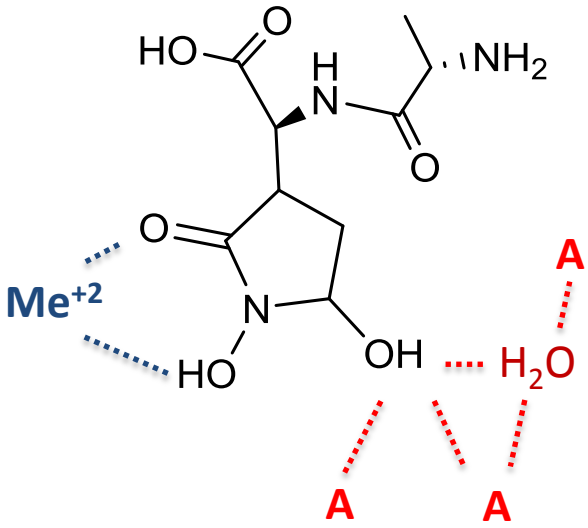

Supplementary Figure 3: *Structural analogues of SF2312 as inhibitors of other Enolase superfamily members.* The natural antibiotic Alahopcin shares the five membered hydroxyl hydroxamate structure with SF2312. The target of Alahopcin has not been identified. We propose that Alahopcin inhibits a member of the Enolase superfamily of enzymes, with the hydroxamate chelating a metal ion (Me^{+2}) and the hydroxyl coordinating with hydrogen bond acceptors, which are known to be conserved in Enolase superfamily members.

Supplementary Figure 4

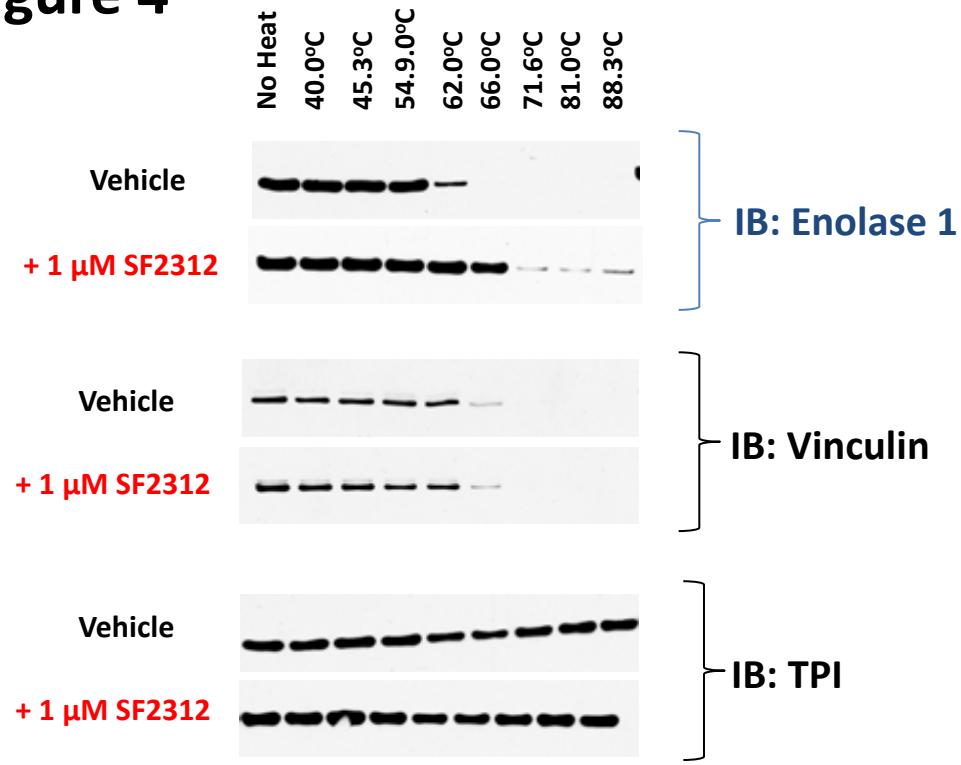

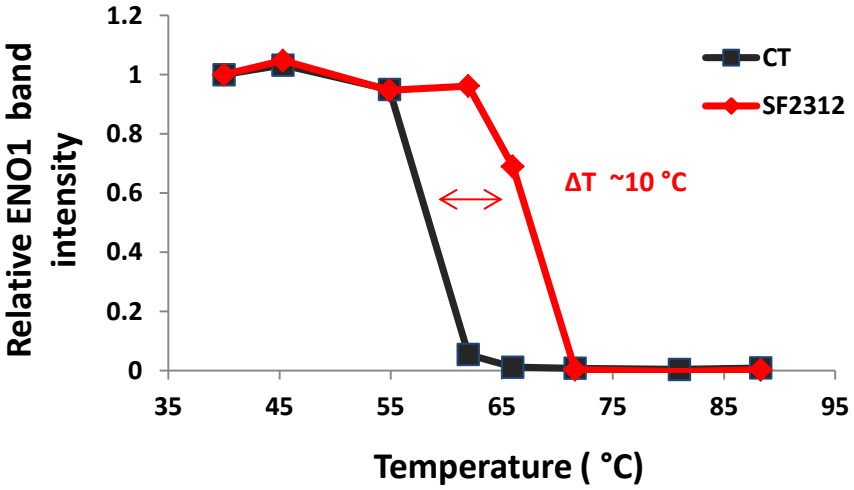

Supplementary Figure 4: *SF2312 stabilizes Enolase 1 against thermal denaturation.* Native lysates of the D423 cell lines overexpressing ENO1 were incubated with SF2312 or vehicle and subjected to thermal denaturation with the supernatant centrifuged to precipitate denatured protein. The supernatant was immunoblotted against ENO1 and the band intensity plotted as a function of temperature (lower panel). As control, lysates were blotted against Vinculin (VIN) and Triosephosphate isomerase (TPI). SF2312 treatment shifted the thermal denaturation curve of ENO1 by ~10 ° C, but was without effect on the negative controls, Vinculin and TPI. The experiment was independently reproduced once.

Supplementary Figure 5

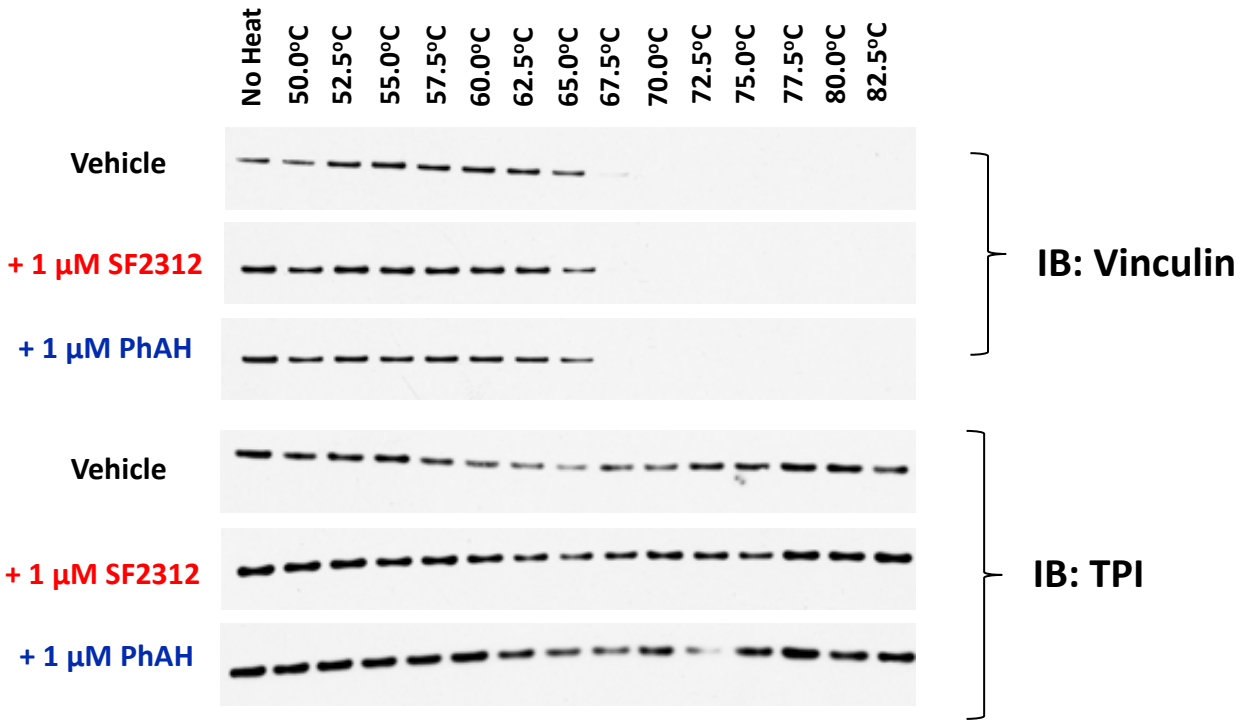

Supplementary Figure 5: *SF2312 has no effect on thermal denaturation on proteins other than Enolase.* Native lysates of the D423 cell lines overexpressing ENO2 were incubated with SF2312, PhAH or vehicle and subjected to thermal denaturation with the supernatant centrifuged to precipitate denatured protein. The supernatant was immunoblotted against ENO2 and the band intensity plotted as a function of temperature (Figure 2). As control, the same lysates were blotted against Vinculin (VIN) and Triosephosphate isomerase (TPI). SF2312 treatment shifted the thermal denaturation curve of ENO2, but was without effect on the negative control, Vinculin and TPI. The experiment was independently reproduced six times.

Supplementary Figure 6

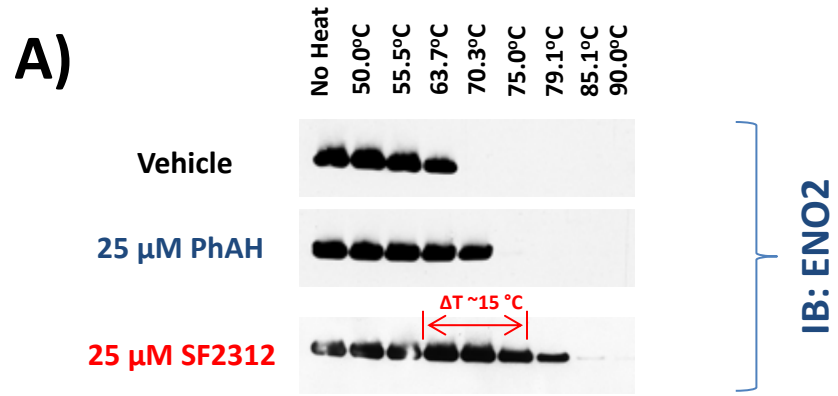

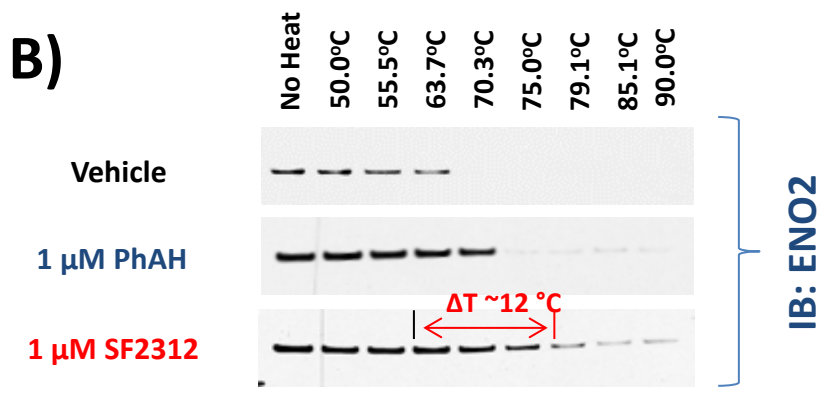

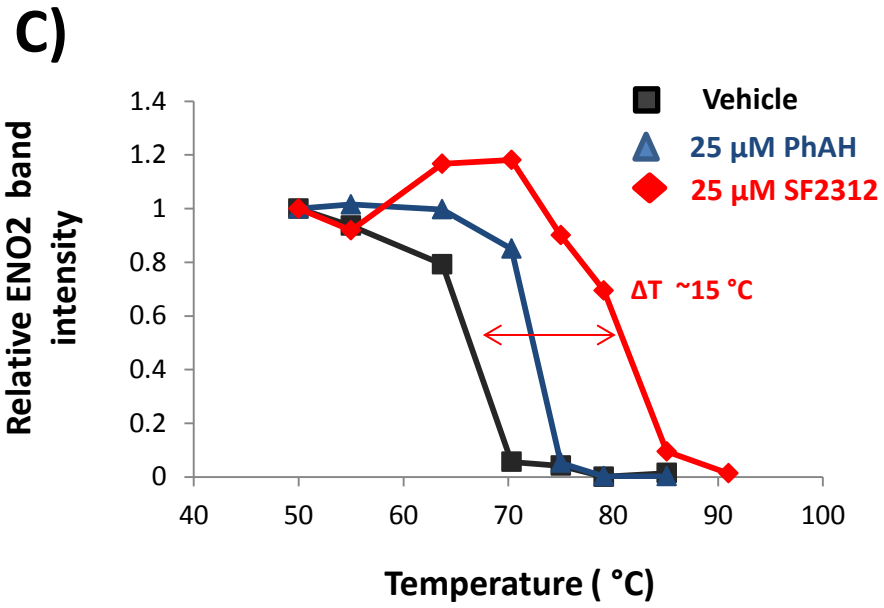

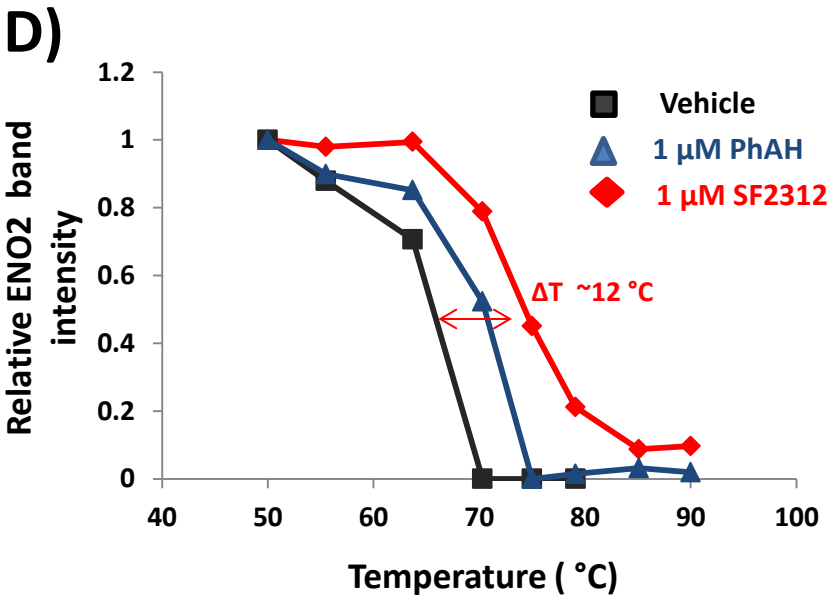

Supplementary Figure 6: *SF2312 stabilizes recombinant human Enolase 2 against thermal denaturation.* Purified *E. coli* expressed ENO2 was incubated with SF2312, PhAH or vehicle and subjected to thermal denaturation with the supernatant centrifuged to precipitate denatured protein. The supernatant was immunoblotted against ENO2 (**Panel A, B**) and the band intensity plotted as function of temperature (**Panel C, D**). Experiments in Panels A,C were conducted with 225 nM recombinant ENO2 protein and 25 µM of inhibitors, while experiments in Panels B,D were conducted with 9 nM recombinant protein and 1 µM of inhibitors. SF2312 treatment shifted the thermal denaturation curve by >12 ° C, considerably more than that observed with the same concentration of PhAH. The experiment was independently reproduced twice. Representative blots are shown.

Supplementary Figure 7

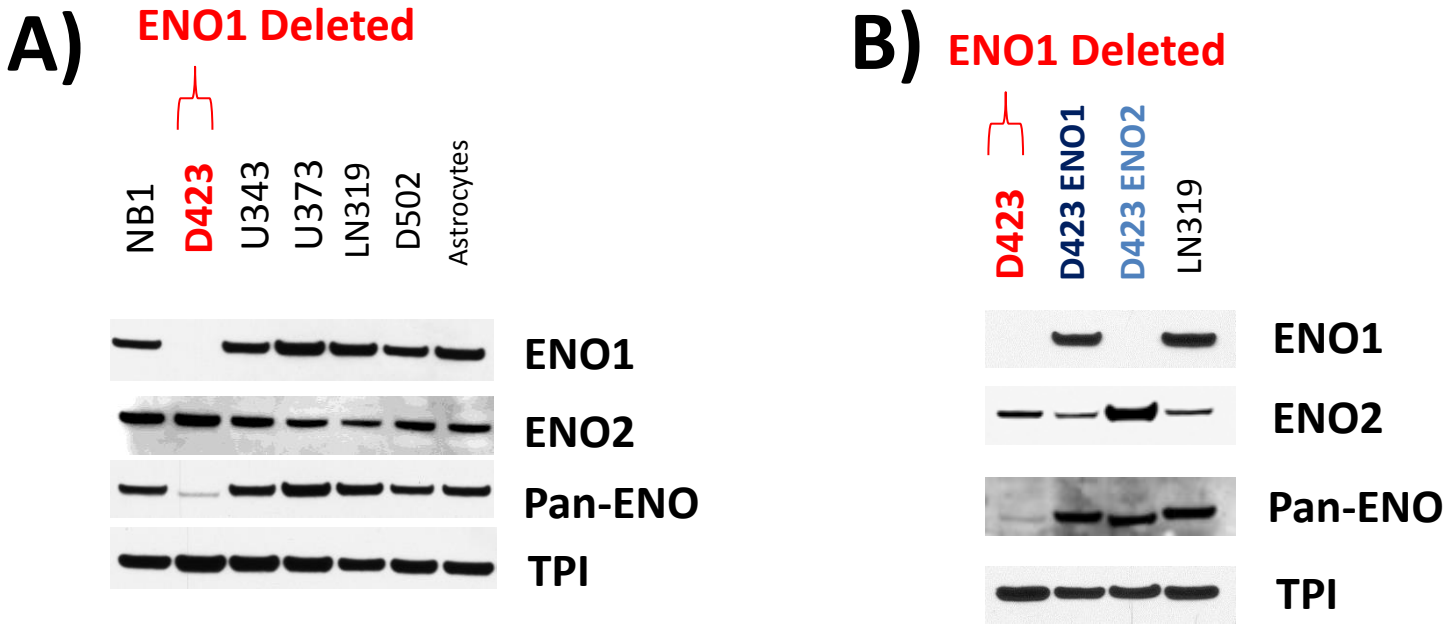

Supplementary Figure 7: *Expression of Enolase in ENO1-deleted, ENO1-rescued and ENO2-rescued glioma cells.* The expression of ENO1, ENO2 and total Enolase (Pan-ENO) was determined by immunoblotting in a panel of glioma cell lines (**Panel A**) and in D423 *ENO1*-deleted, rescued by re-expression of ENO1 (D423 ENO1, dark blue) or overexpression of ENO2 (D423 ENO2, light blue) glioma cells with reference to the *ENO1*-intact LN319 glioma line (**Panel B**). TPI was used as a loading control. ENO1 was undetectable in the D423 *ENO1*-deleted cell line (**Panel A**), while ENO2 expression was similar to the other cell lines in the panel. Total expression of Enolase, as determined by the pan-ENO antibody, was dramatically reduced in D423 *ENO1*-deleted cells. Ectopic expression of ENO1 (D423 ENO1, **Panel B**) or overexpression of ENO2 (D423 ENO2), restored total Enolase expression (Pan-ENO, **Panel B**) to levels similar to that in the *ENO1*-intact LN319 glioma cell line. The western blots were reproduced three times and twice for panels, A and B, respectively.

Supplementary Figure 8

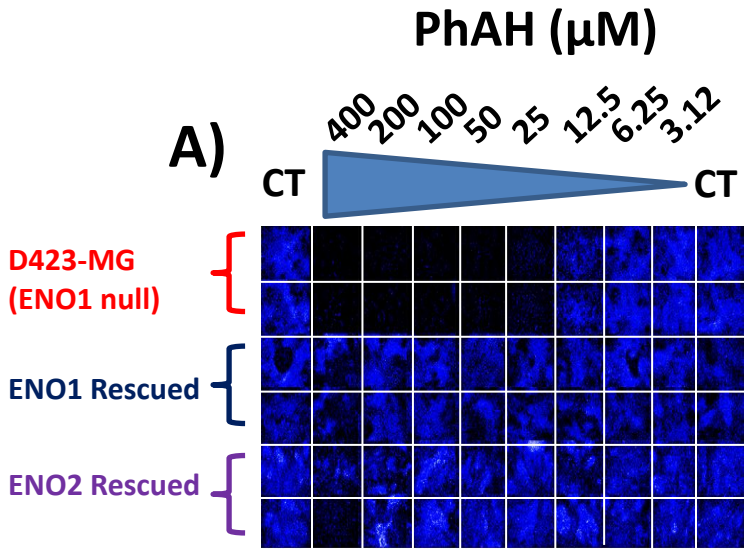

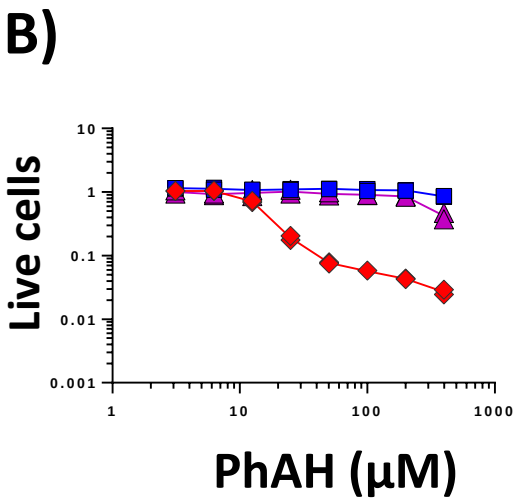

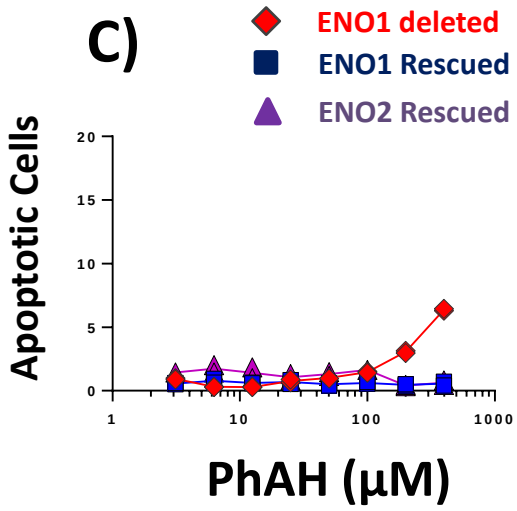

Supplementary Figure 8: *Selective toxicity of PhAH to ENO1 deleted glioma cells.*
In a parallel experiment with SF2312 (Figure 4), PhAH was tested for its effect on cell proliferation and cell death in D423 *ENO1*-deleted (red), D423 isogenic controls expressing ENO1 (dark blue) or overexpressing ENO2 (light purple). Cells were treated with varying concentrations of inhibitors as indicated in µM, with the first and the last column servicing as vehicle controls. After 2-weeks of treatment, plates were assayed for cell number (total cell number, Hoechst 33342) and apoptosis (YO-PRO®-1 positive cells) using the Operetta® High Content Imaging System. Panels to the left show 96-well plates treated with PhAH (**Panel A**) stained with Hoechst; the extent of blue color indicates cell number. Quantified results for cell number and apoptosis as a function of inhibitor concentration are presented in **Panels B and C**, respectively; each treatment condition was performed in duplicate and expressed as a function of vehicle control (N = 4). The experiment comparing the selective toxicity of PhAH to D423 *ENO1*-deleted cells was repeated at least four times.

Supplementary Figure 9

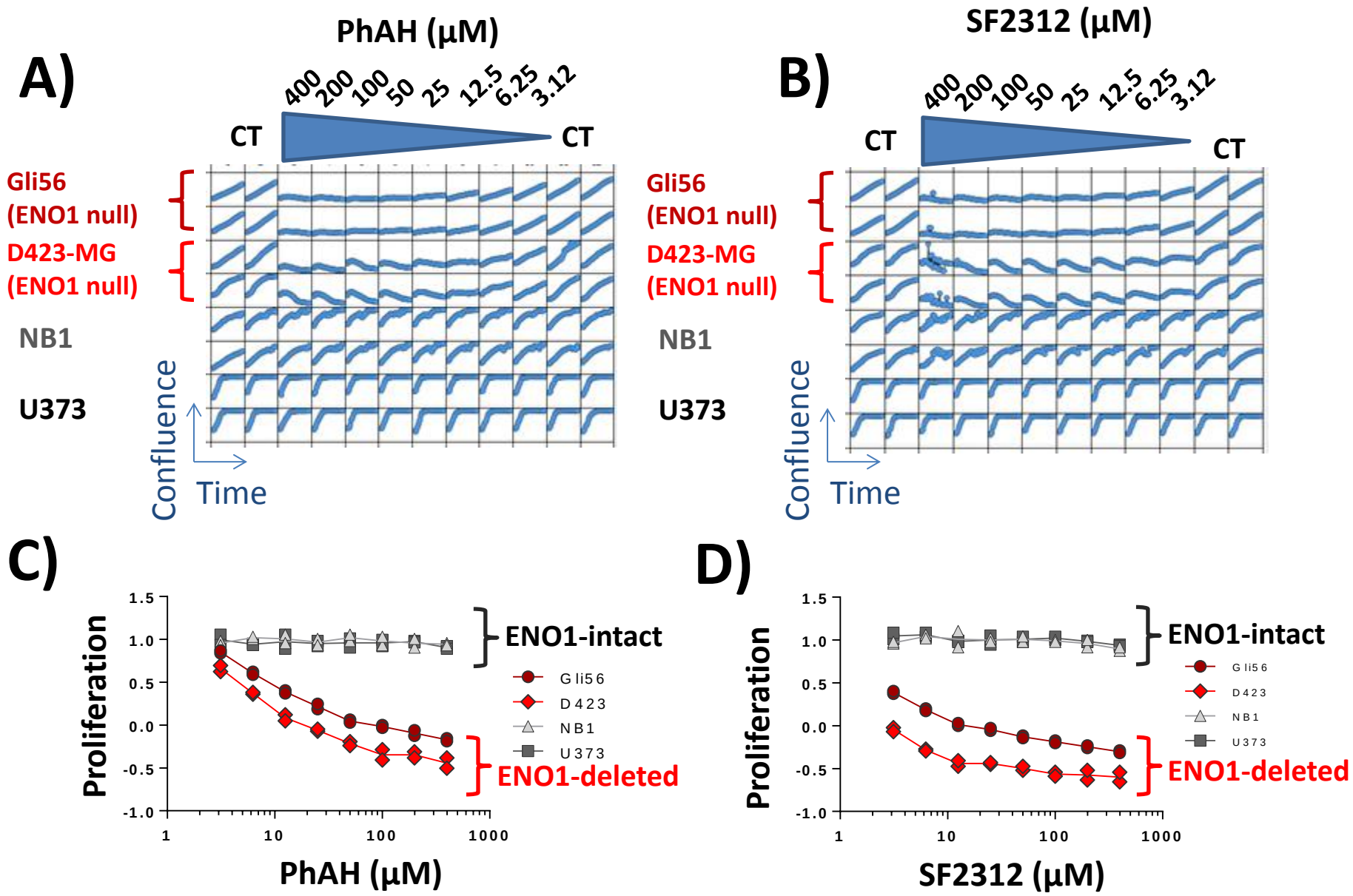

Supplementary Figure 9: *SF2312 selectively inhibits the proliferation of ENO1-deleted glioma cells.* Gli56 (dark red) and D423 (red) *ENO1* deleted and non-deleted (U373, NB1) cell lines were treated with varying doses of SF2312 (**Panel B**) or PhAH (**Panel A**) for a total of ten days. Cell proliferation was measured using the Incucyte with growth curves shown in blue traces (y-axis, cell confluence, x-axis, time). Steep rising curves indicate increases in confluence and proliferation. Flat curves indicate steady confluence and inhibited proliferation, while declining curves indicate cell death. In **Panels C** (PhAH) and **D** (SF2312), for each cell line, proliferation was quantified (N=2 replicates) and expressed relative to vehicle controls (N=4) as a function of inhibitor concentration. The experiment was independently reproduced at least 3 times.

Supplementary Figure 10

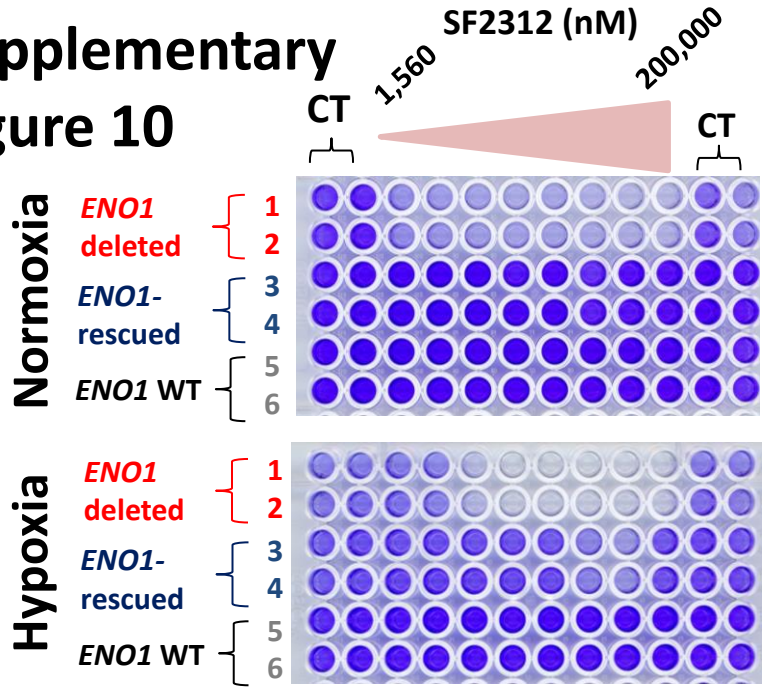

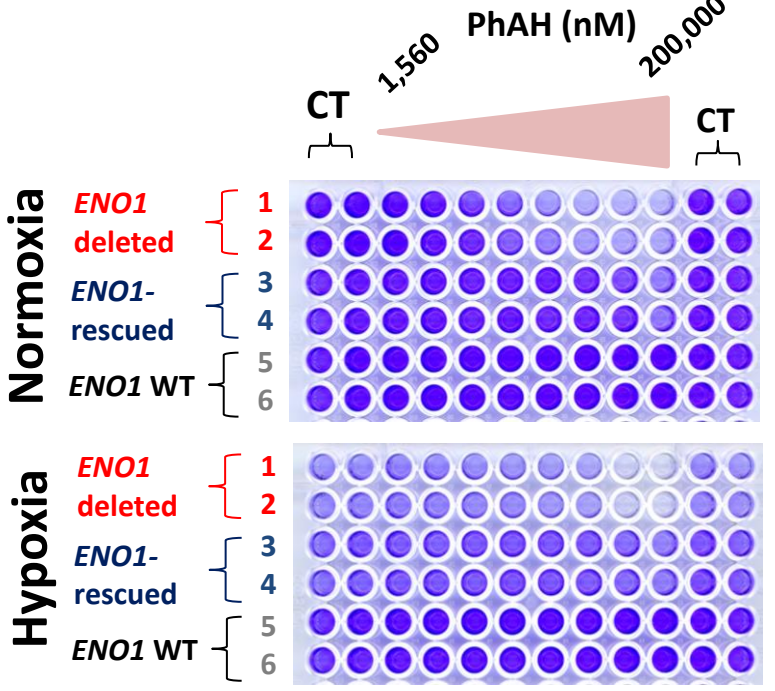

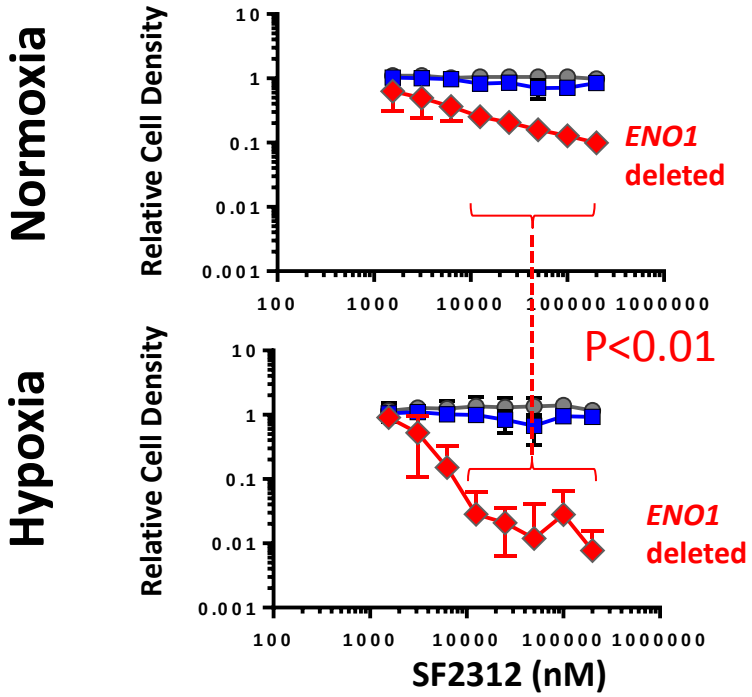

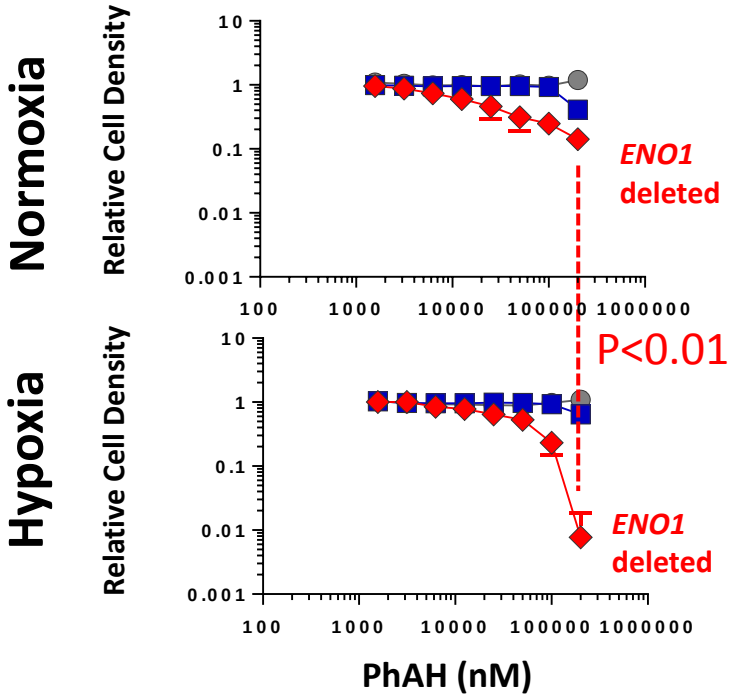

Supplementary Figure 10: *Toxicity of SF2312 against ENO1 deleted glioma cells is increased under hypoxia.* D423 (*ENO1*-deleted, red diamonds, rows 1,2), D423 ENO1 (*ENO1*-rescued, blue squares, rows 3,4) and LN319 (*ENO1*-WT, grey circles, rows 5,6) glioma cells were treated for 72 hours with 2-fold dilution series of SF2312 (left side panels), PhAH (right side panels) or vehicle control, under either convention culture conditions (Normoxia) or 0.1% O2 (Hypoxia). Cell density was quantified by crystal violet and expressed relative to vehicle control (y axis, $\log_{10}$) as a function of inhibitor concentration (in nM, $\log_{10}$). Representative 96-well plates are shown, with quantification of N = 8 wells for SF2312 and N = 10 for PhAH (mean ± S.D.). Significant differences between hypoxia and normoxia are indicated. For SF2312, inhibitor concentrations above 6250 nM showed statistically significantly lower relative cell density under hypoxia (at least $P<0.01$, unpaired, two-tailed t-test with Bonferroni correction), whilst for PhAH, this was only the case at 200,000 nM. The experiment was reproduced independently once.

Supplementary Figure 11

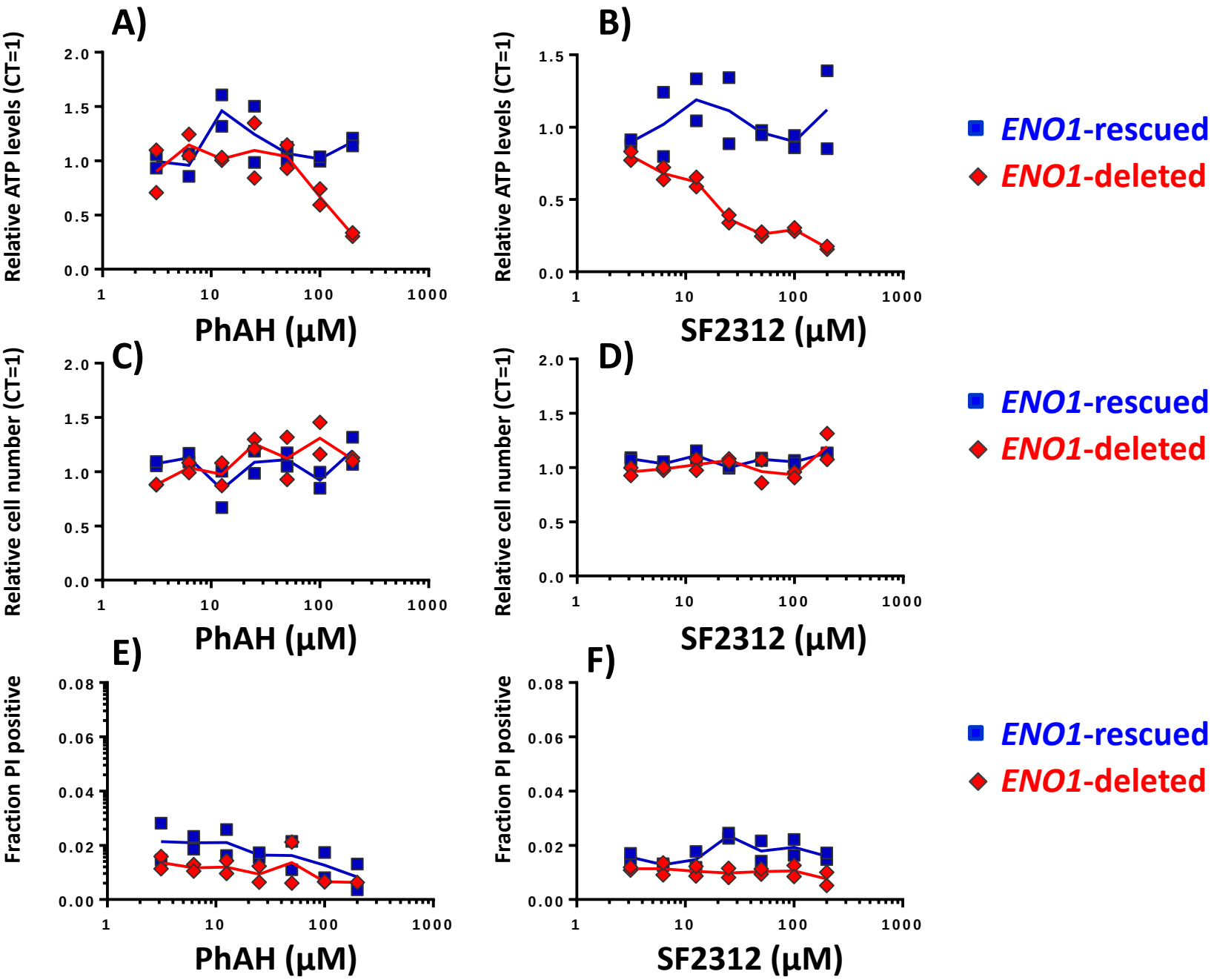

Supplementary Figure 11: *SF2312 selectively depletes ATP in ENO1-deleted glioma cells.* D423 *ENO1*-deleted (red diamonds) and isogenic *ENO1*-rescued control (blue squares) glioma cells were treated for 8 hours with PhAH (**Panels A**, **C**, **E**) or SF2312 (**Panels B**, **D**, **F**) at concentrations indicated in the x-axis and the effects on ATP (**Panels A, B**), Cell number (**Panels C, D**) and Cell death (**Panels E**, **F**) were determined. ATP was measured using the Cell-Titer Glow assay. Each experimental condition was assayed in duplicate wells expressed as function of N = 8 vehicle treated wells, with mean plotted as a line. Cell number as measured nuclei measured via Hoechst 33342 using the Operetta®(**Panels C, D**). The extent of cell death (**Panels E, F**) was expressed as the fraction of propidium iodide positive nuclei. At 8 hours of treatment, SF2312 treatment led to a dose dependent depletion of ATP in *ENO1*-deleted but not rescued glioma cells. The experiment was independently reproduced once.

Supplementary Figure 12

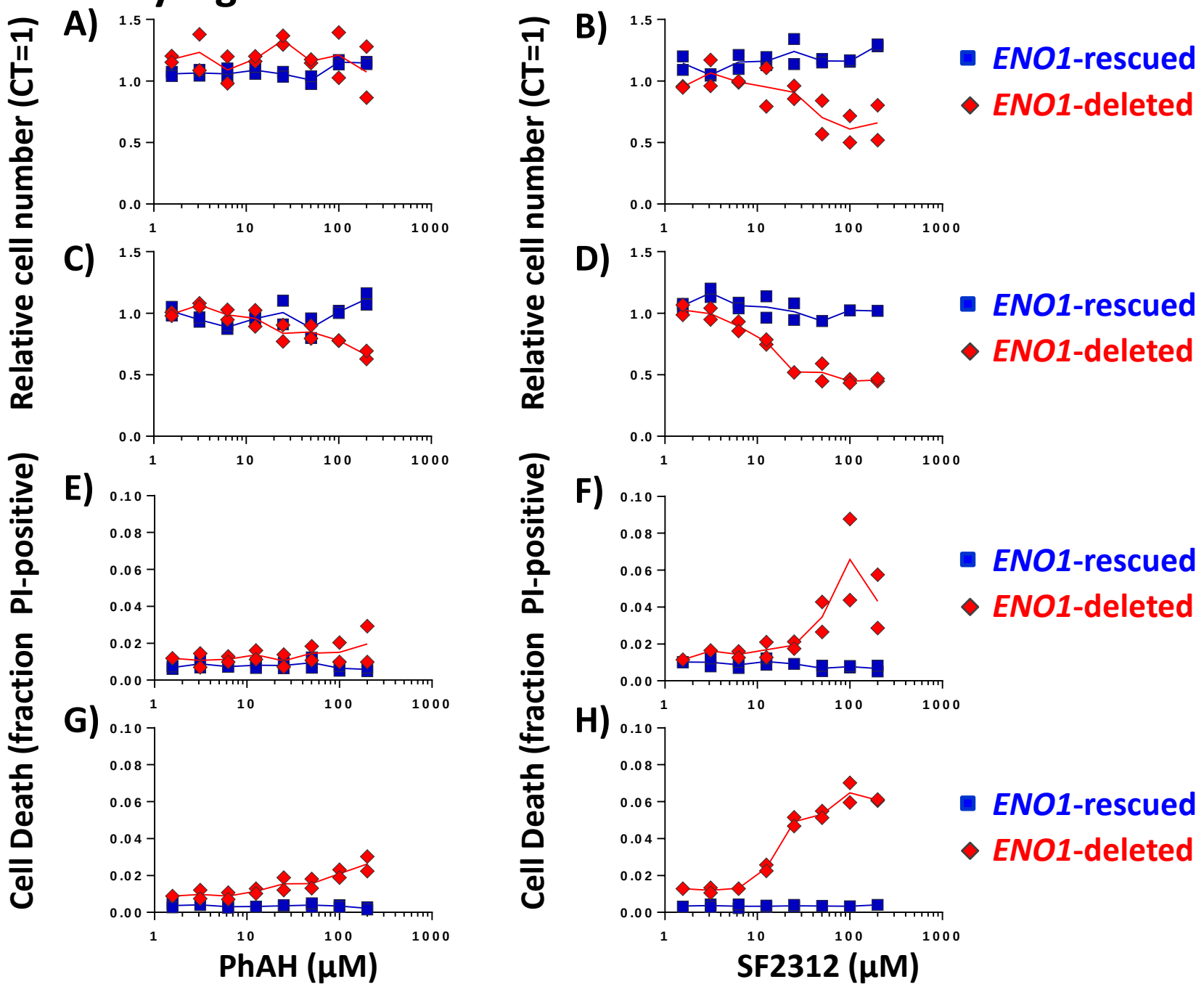

Supplementary Figure 12: *Effect of SF2312 and PhAH on cell death and cell number in ENO1-deleted and isogenic rescued glioma cells.* D423 *ENO1*-deleted (red diamonds) and isogenic *ENO1*-rescued control (blue squares) glioma cells were treated for 24 hours (**Panels A, B, E, F**) or 48 hours (**Panels C, D, G, H**) with PhAH (**Panels A, C, E, G**) or SF2312 (**Panels B, D, F, H**) at concentrations indicated in the x-axis and the effects on Cell number (**Panels A, B, C, D**) and Cell death (**Panels E, F, G, H**) were determined in 96-well format. Cell number as measured nuclei measured via Hoechst 33342 using the Operetta®. Each experimental condition was performed in duplicate wells with each datapoint representing a single well expressed relative to eight untreated control wells, with mean plotted as a line (**Panels A, B, C, D**). The extent of cell death (**Panels E, F, G, H**) was expressed as the fraction of propidium iodide positive nuclei. SF2312 treatment led to a time and dose dependent induction of cell death in *ENO1*-deleted but not rescued cells. Cell death in response to PhAH was considerably weaker. The experiment was independently reproduced once.

Supplementary Figure 13

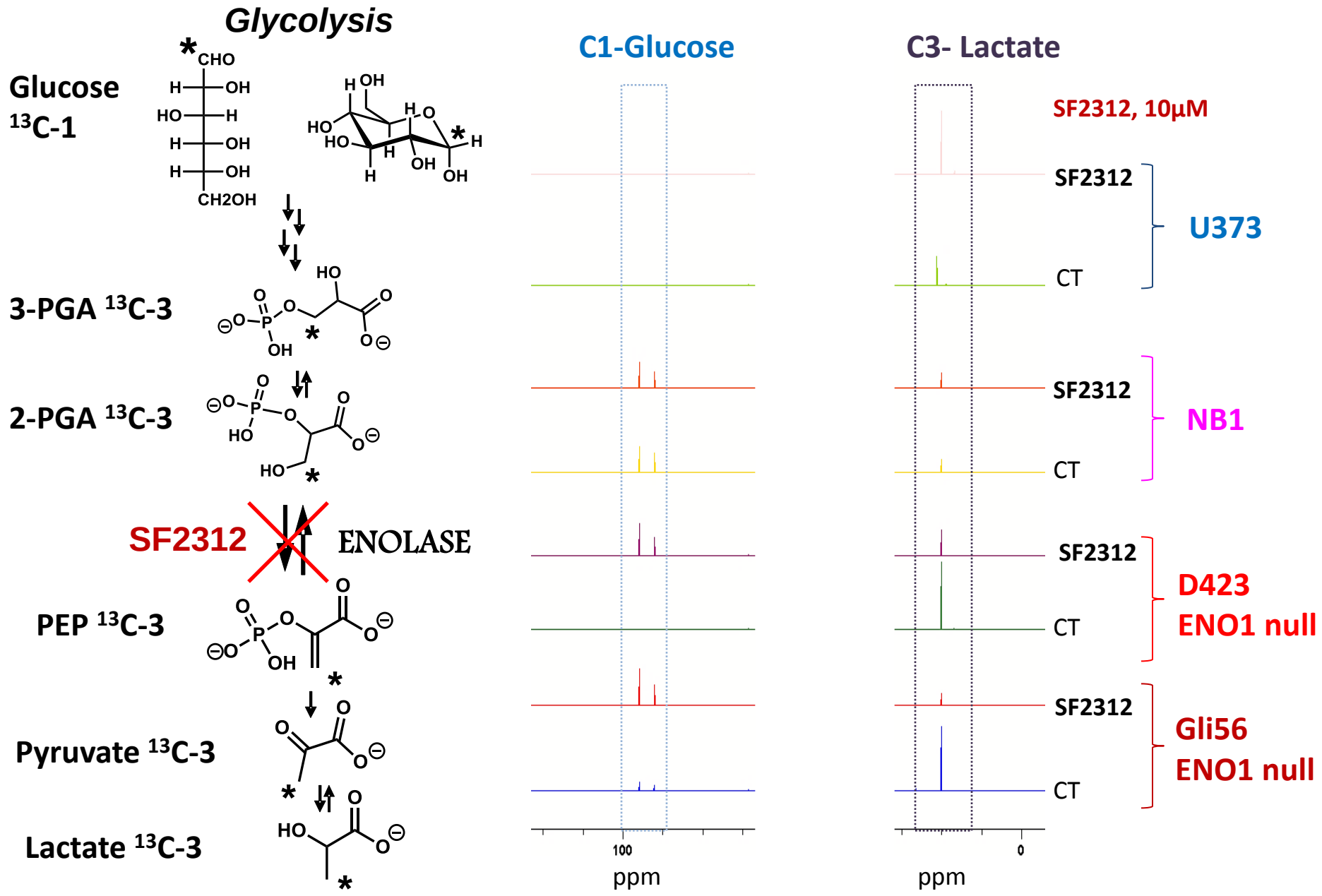

Supplementary Figure 13: *SF2312 selectively inhibits glycolysis in ENO1-deleted glioma cells.* Gli56 and D423 *ENO1*-deleted and non-deleted (U373, NB1) cells were supplemented with ^{13}C-1 labeled glucose (indicated by asterisk*) treated with 10 µM of SF2312 for four days. Conditioned media was harvested after four days and extracted and scanned by ^{13}C NMR in proton decoupled mode. Large peaks at ~97 and 93 ppm correspond to the isomers of glucose and at ~20 ppm to the C3 of lactate. In the absence of treatment, glucose peaks disappeared with concomitant appearance of lactate peaks. Treatment with SF2312 inhibited the disappearance of glucose and the appearance of lactate peaks, but only in the D423 and Gli56 ENO1 deleted cells, indicating selective inhibition of glycolysis in these cell lines. The experiment was reproduced once, with identical results.

Supplementary Figure 14

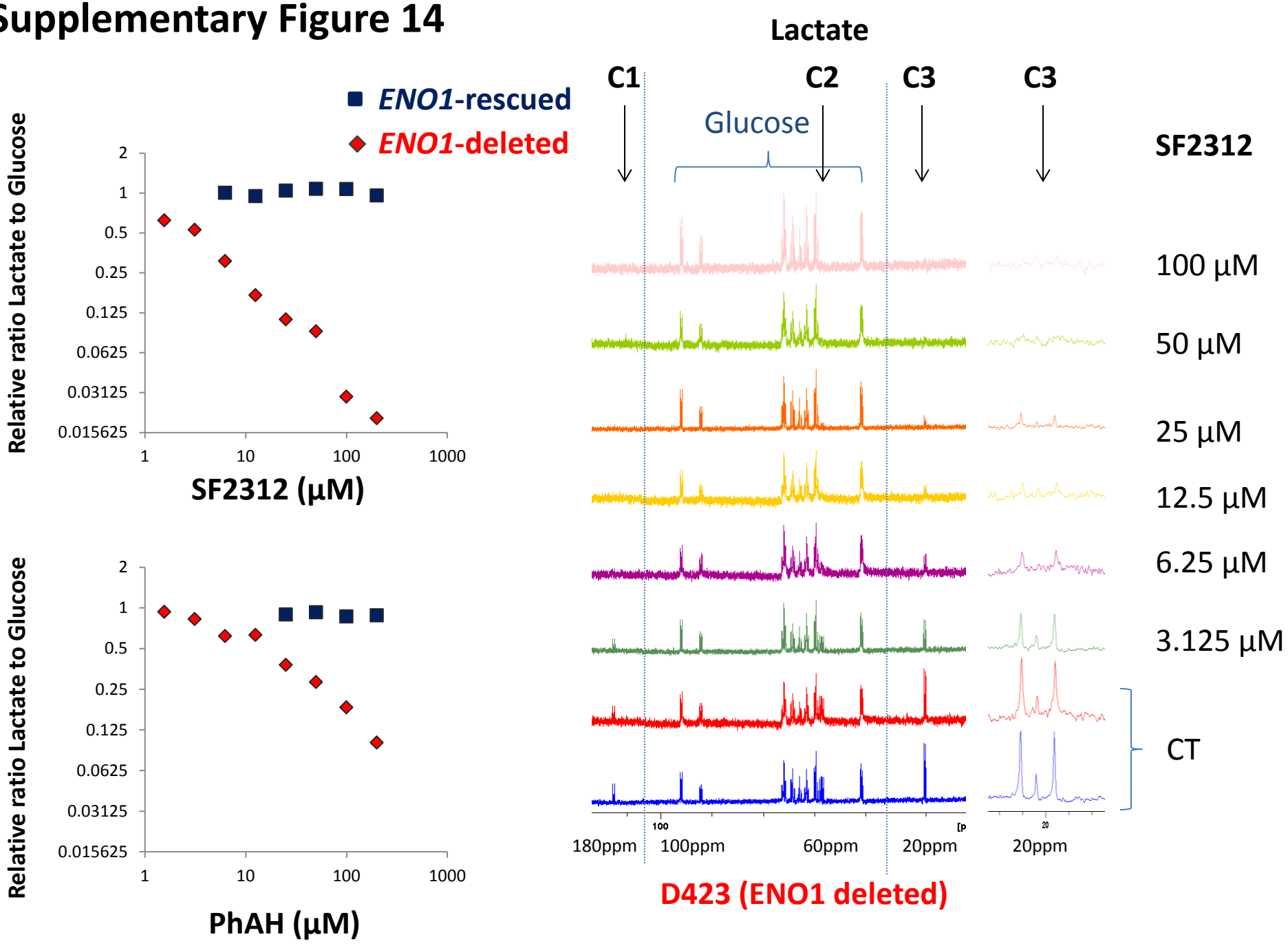

Supplementary Figure 14: *SF2312 selectively inhibits conversion of uniformly labeled ^{13}C-glucose to ^{13}C-lactate in ENO1-deleted glioma cells.* D423 *ENO1*-deleted (red diamonds) and D423 ectopically rescued cells (D423 ENO1; blue squares) were treated with varying doses of SF2312 and PhAH in media containing 10 mM ^{13}C-uniformly labeled glucose. Forty-eight hours later, media was collected and ^{13}C-NMR scanned. The right panel shows raw traces of media from D423 *ENO1*-deleted cells treated with different concentrations of SF2312. The peaks corresponding to glucose (from 100 to 50 ppm, right panel) are bracketed, while the peaks corresponding to the C1, C2, and C3 atoms of lactate are pointed out with black arrows. A zoom in of the C3 lactate peak is shown. The ratio of the integral of lactate to the integral of glucose was determined, normalized with respect to vehicle treated control (y-axis, log2 scale), and plotted as a function of PhAH or SF2312 concentration (x-axis, left panels). Concentrations of SF2312 as low as 6.25 µM were sufficient to decrease the ratio of ^{13}C Lactate/^{13}C glucose by 70% whilst 50 µM of PhAH were necessary for a similar level of inhibition in *ENO1*-deleted glioma cells. In contrast, even at 200 µM, neither PhAH nor SF2312 decreased lactate/glucose in D423 *ENO1*-rescued glioma cells. This experiment was reproduced once.

Supplementary Figure 15

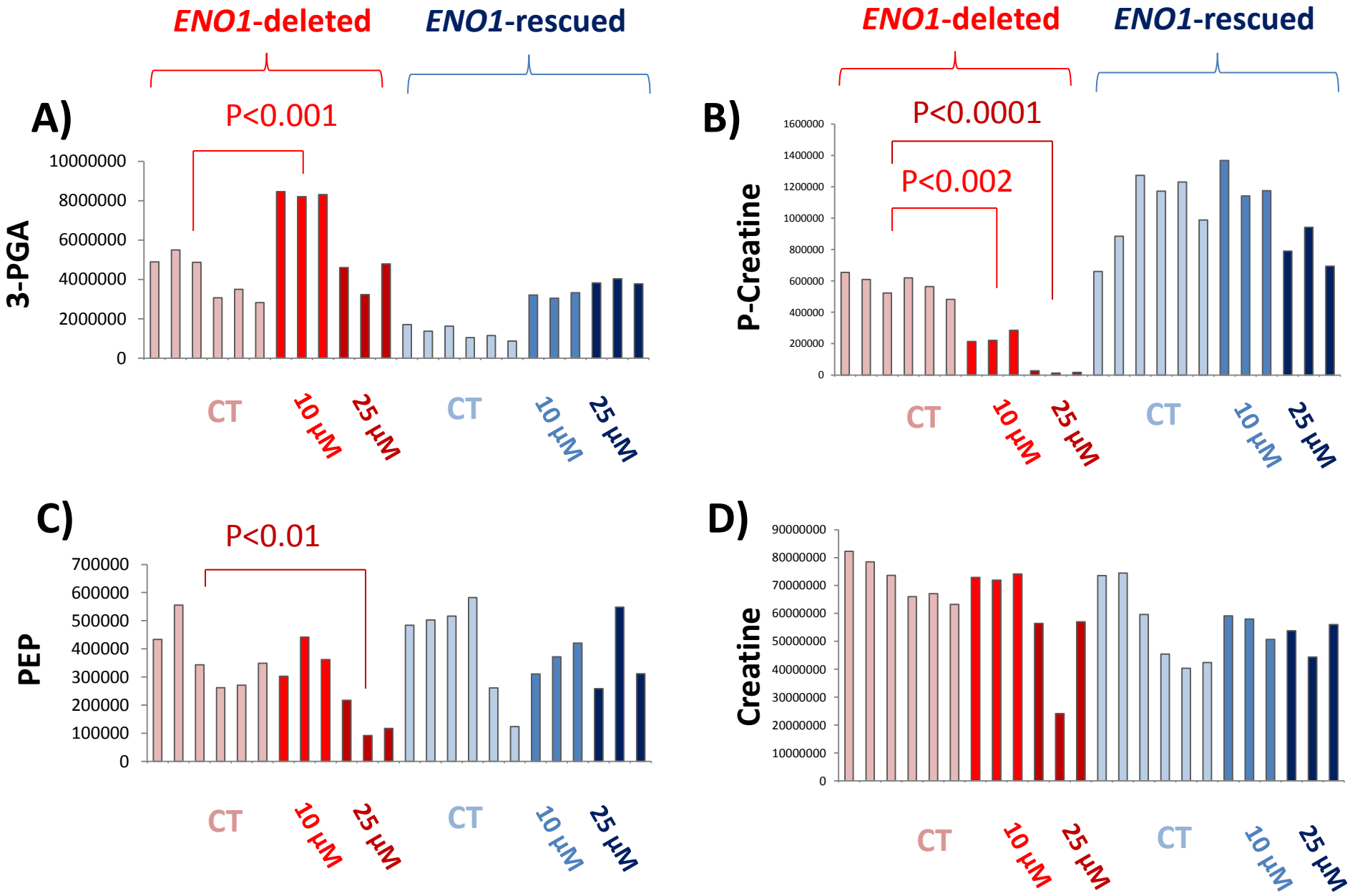

Supplementary Figure 15: *Effects of SF2312 on glycolytic intermediates immediately around the Enolase step raw data.* Phosphoenol pyruvate (PEP, **Panel B**), 3-Phosphoglycerate (3-PGA, **Panel A**), Creatine (**Panel C**) and Phosphocreatine (P-Creatine, **Panel D**) were measured by mass spec as described in methods, in response to 10 or 25 µM SF2312, in either *ENO1*-deleted, or *ENO1*-rescued D423 glioma cells. Units in y-axis are peak area intensities calculated from raw mass spec total ion current. Each bar represents a separate biological replicate. Ratios of 3-PGA/PEP and P-Creatine/Creatine are shown in Figure 4. Significant differences by unpaired t-test with Bonferroni correction are indicated.

Supplementary Figure 16

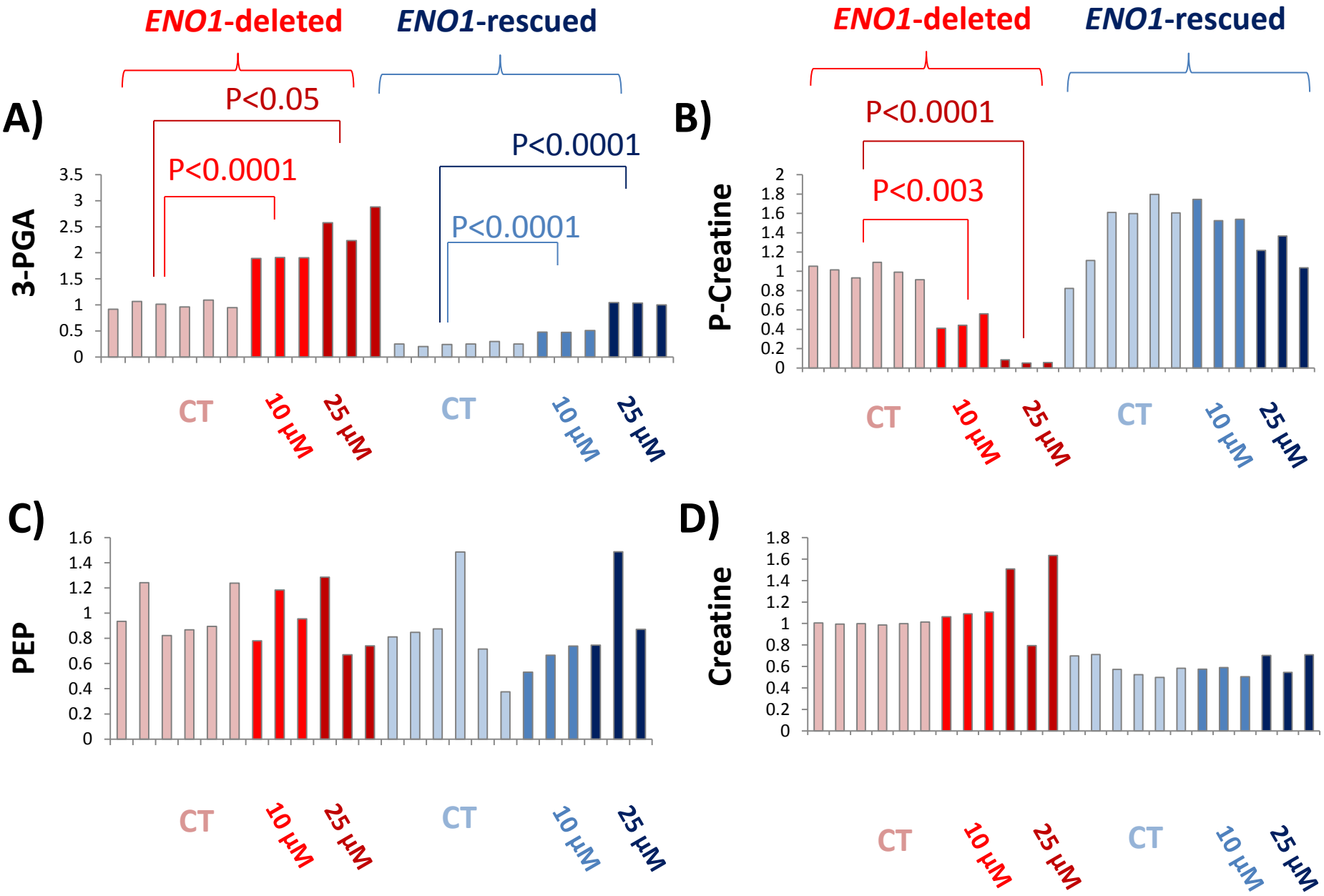

Supplementary Figure 16: *Effects of SF2312 on glycolytic intermediates immediately around the Enolase step normalized.* Phosphoenol pyruvate (PEP, **Panel B**), 3-Phosphoglycerate (3-PGA, **Panel A**), Creatine (**Panel C**) and Phosphocreatine (P-Creatine, **Panel D**) were measured by as described in methods, in response to 10 or 25 µM SF2312, in either *ENO1*-deleted, or *ENO1*-rescued D423 glioma cells. Data for each metabolite was normalized to total mass spec ion current and expressed relative to control D423 *ENO1*-deleted (y-axis). Each bar represents a separate biological replicate. Significant differences by unpaired t-test with Bonferroni correction are indicated.

Supplementary Figure 17

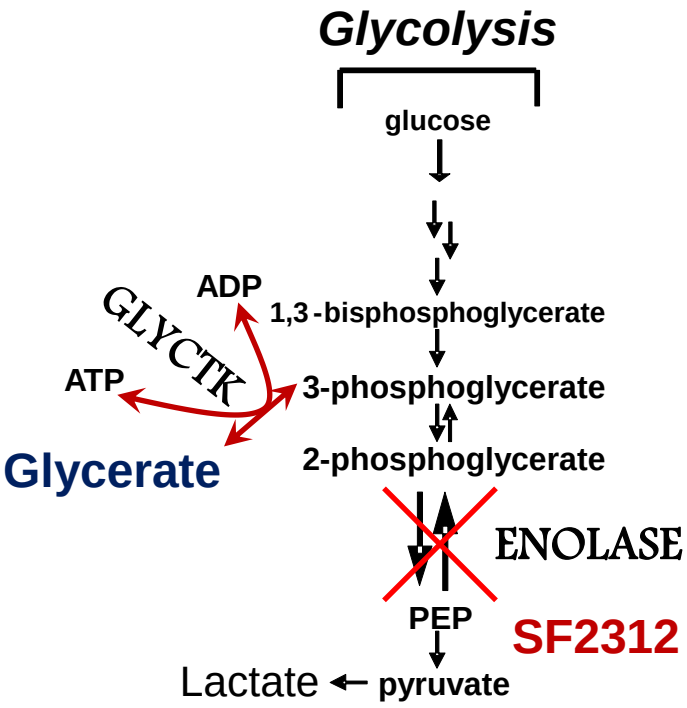

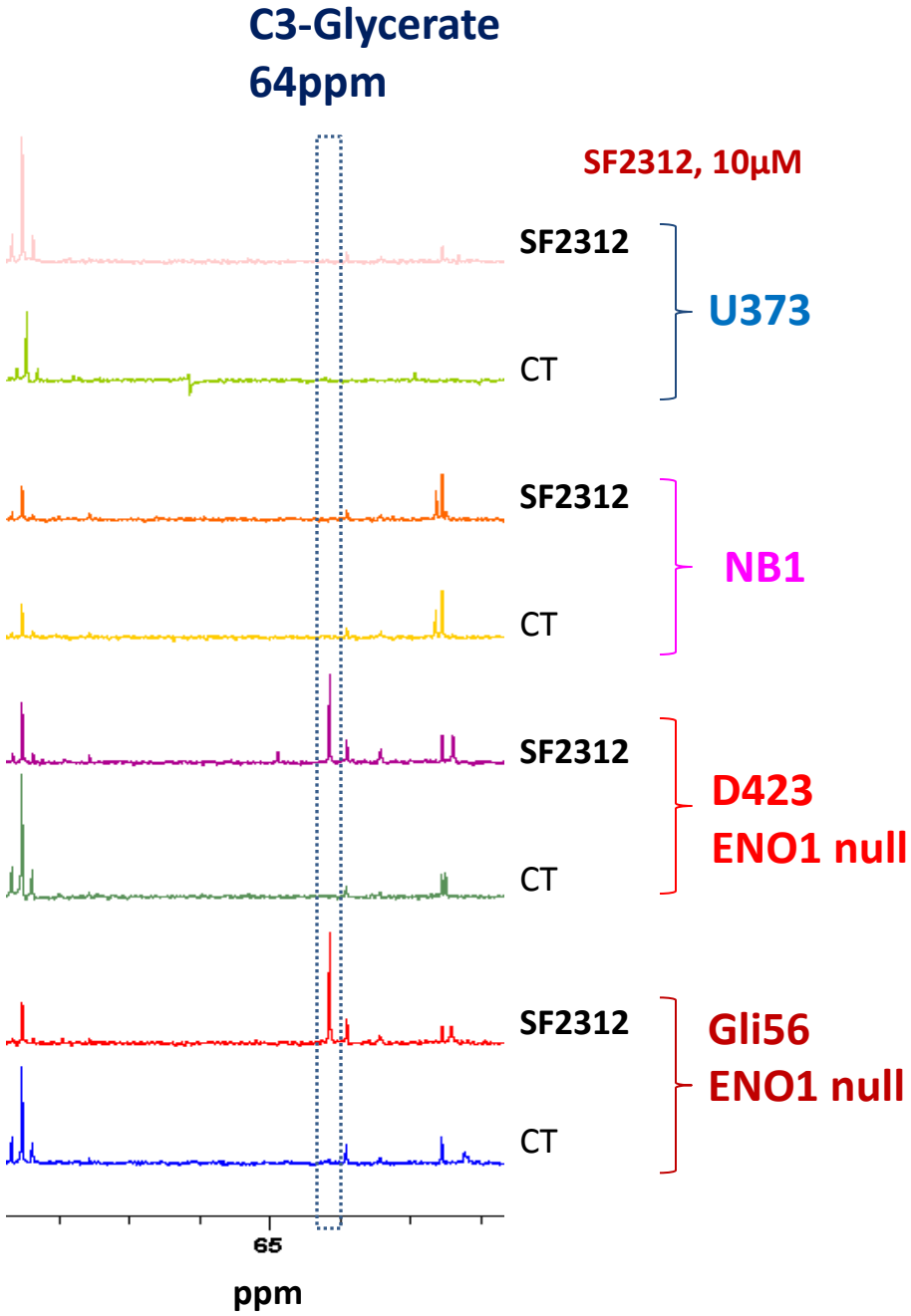

Supplementary Figure 17: *SF2312 treatment leads to a build-up of intermediates upstream of Enolase. ENO1*-intact (U373, NB1) and *ENO1*-deleted (D423, Gli56) glioma cells were grown in ^{13}C-1 glucose media and treated with 10 µM SF2312. Media was extracted and scanned by proton-decoupled ^{13}C NMR. In *ENO1*-deleted but not in *ENO1*-intact cell lines, SF2312 treatment led to the appearance of a distinct peak at 64 ppm. This is consistent with secretion of glycerate into the media, which we suggest forms from 3-phosphoglycerate by the action of glycerate kinase (GLYCTK) or by spontaneous hydrolysis as a result of accumulation of substrates (phosphoglycerate) upstream of Enolase. The experiment was reproduced once, a representative trace is shown.

Supplementary Figure 18

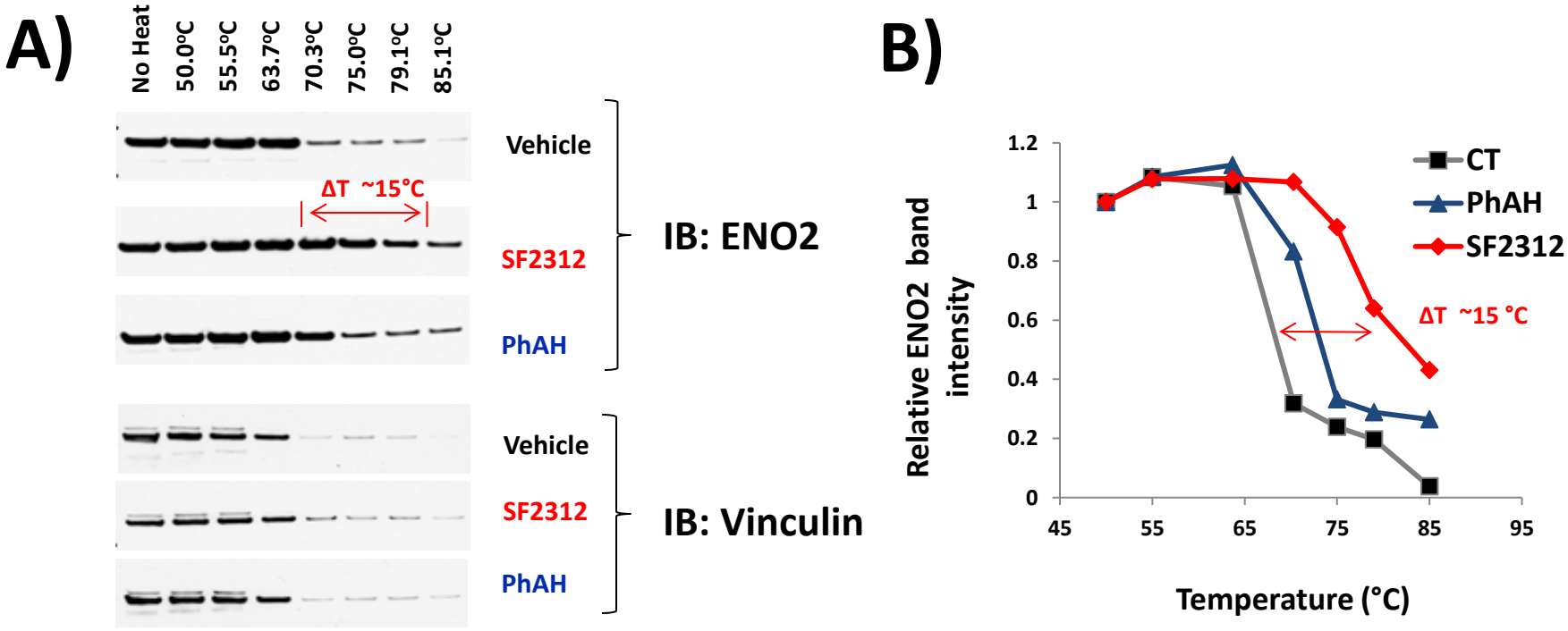

Supplementary Figure 18: *Thermal stabilization of ENO2 by SF2312 and PhAH in intact glioma cells.* Thermal shift Assays in D423 cells overexpressing ENO2 were performed as detailed in methods. Intact glioma cells were treated with 100 μM PhAH, SF2312 or vehicle and individual aliquots heated at the temperatures as indicated. Lysates were generated and supernatant was immunoblotted for ENO2 and Vinculin (**Panel A**). Relative intensity of the ENO2 bands was plotted as a function of temperature (**Panel B**). Both PhAH and SF2312 resulted in stabilization of ENO2, with the effect being more dramatic for the later. The experiment was repeated independently once.

Supplementary Figure 19

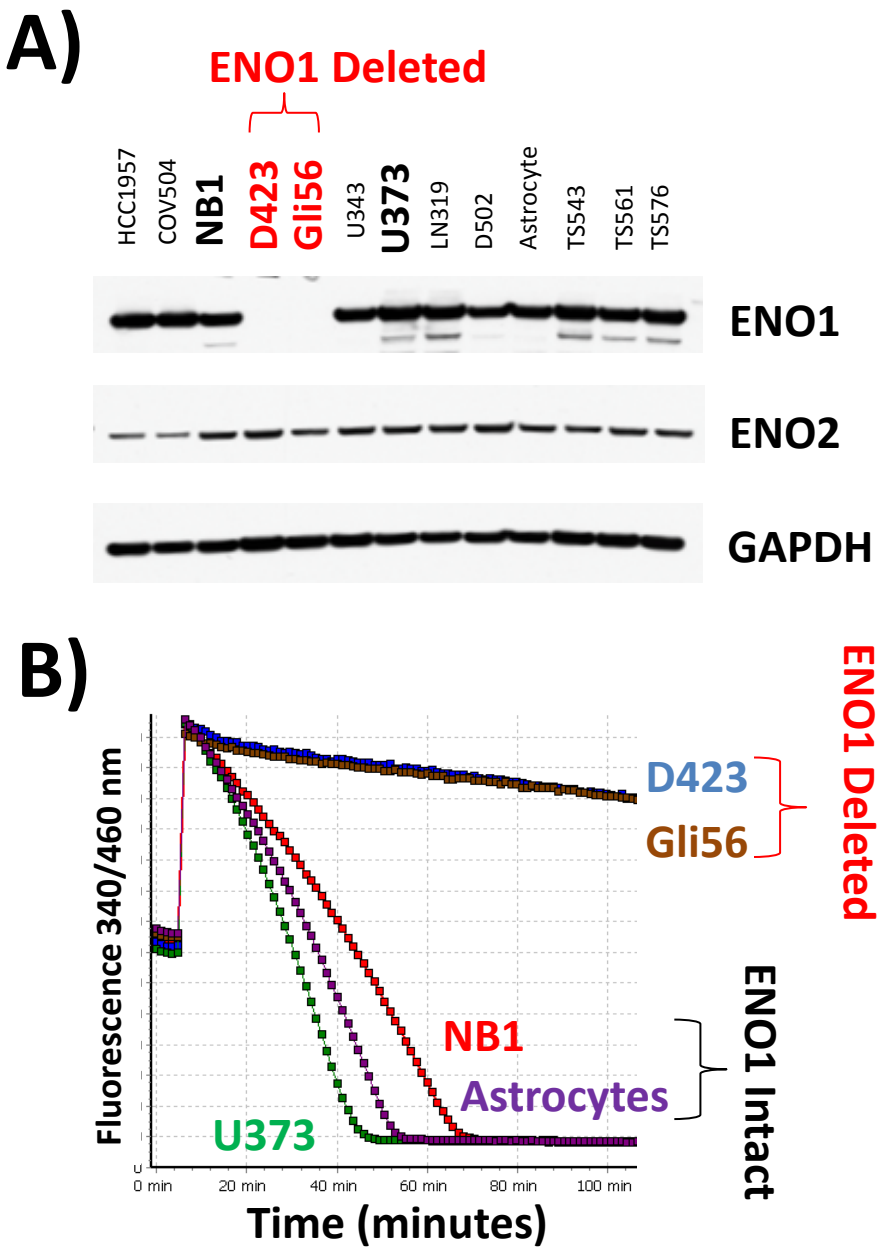

Supplementary Figure 19: *ENO1-deleted glioma cells have profoundly decreased Enolase activity which sensitizes to Enolase inhibitors.* D423 and Gli56 glioma cells carry 1p36 homozygous deletions spanning ENO1 (5). Absence of ENO1 expression in D423 and Gli56 cells was verified by western blot (**Panel A**); despite complete absence of ENO1, levels of ENO2 remained similar to the other cell lines. As a result, D423 and Gli56 *ENO1*-deleted cells are profoundly deficient in Enolase activity as compared to ENO1 intact cells (**Panel B**). Native lysates from D423 (blue trace) and Gli56 (brown trace) *ENO1*-deleted and *ENO1*-intact U373 (green trace) and NB1 (red trace) glioma cells, as well as normal human astrocytes (purple trace), were equalized for protein and Enolase activity was measured using the NADH-linked assay (y-axis, measured fluorescently 340 nm excitation/460 nm emission; see methods). The slope of each trace reflects the level of enolase activity; *ENO1*-intact NB1, U373 and astrocytes have slopes ~10-steeper than *ENO1*-deleted D423 and Gli56, showing that the latter are profoundly deficient in Enolase activity. The western blot (**Panel A**) was reproduced at least three times. Enolase activity (**Panel B**) was reproduced at least twice, a representative trace is shown. The ~90% deficiency in Enolase activity is most likely responsible for the increased sensitivity of *ENO1*-deleted glioma cells towards SF2312 and PhAH, even though neither inhibitor is specific for ENO2 (**Panel C**). Because fewer active sites are present in *ENO1*-deleted cells, small quantities of Enolase inhibitor are sufficient to saturate active sites and inhibit overall Enolase activity below toxic threshold. This shuts down glycolysis, preventing the production of ATP, resulting in bioenergetic failure and cell death. Similar doses of inhibitor show minimal toxicity to *ENO1*-intact cells because even in the present of inhibitor, residual Enolase activity is sufficient to carry out glycolysis.

Supplementary Figure 20

A)

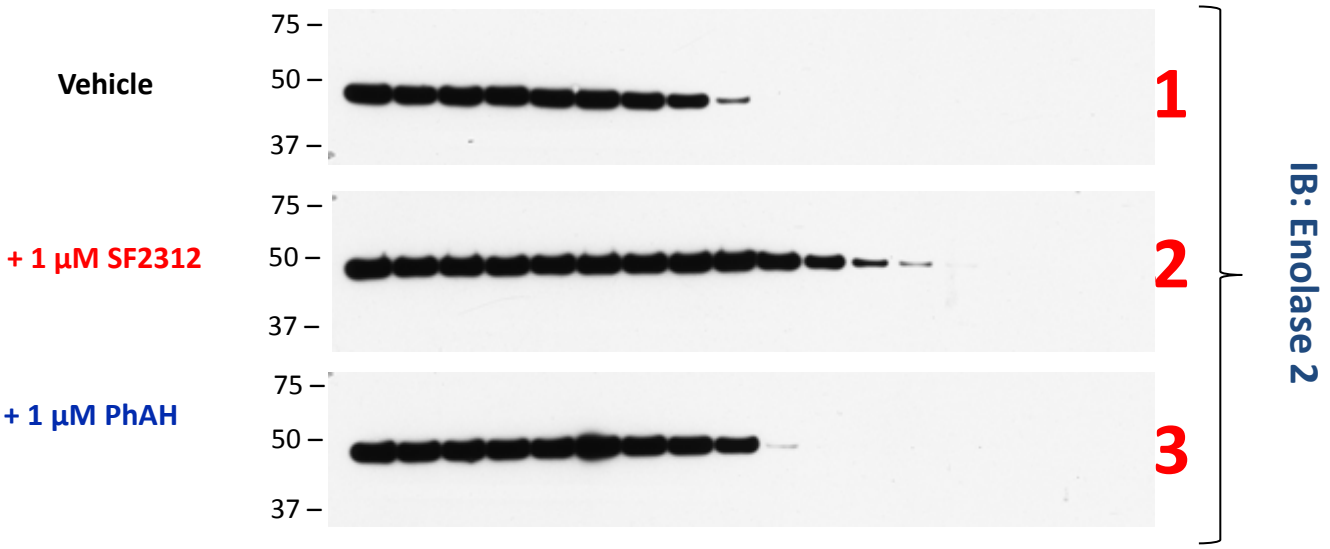

Supplementary Figure 20

B)

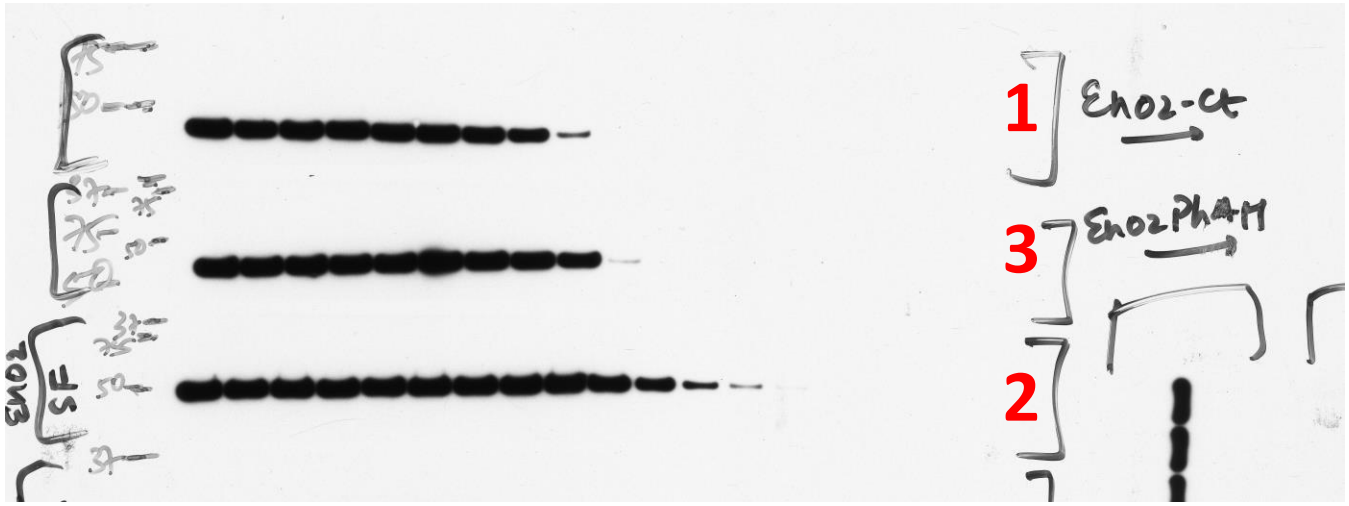

Supplementary Figure 20: *Uncropped western blot scans for Figure 2.* **Panel A**) Partially cropped and size marker annotated western blots; **Panel B**) Raw x-ray film scans with numbers in red indicating the blots shown in figure. Lysates from thermal shift assays were size separated by electrophoresis and transferred to nitrocellulose membranes. The membranes were cut at the 75 kDa and 37 kDa size markers. The high molecular weight (250 – 75 kDa) region was blotted for Vinculin (MW = 130 kDa, Supplementary Figure 22), while the middle (75- 37 kDa) was blotted for ENO2 (MW = 47 kDa), whilst the low molecular weight fragment was blotted for TPI (MW = 25 kDa, Supplementary Figure 22).

Supplementary Figure 21

A)

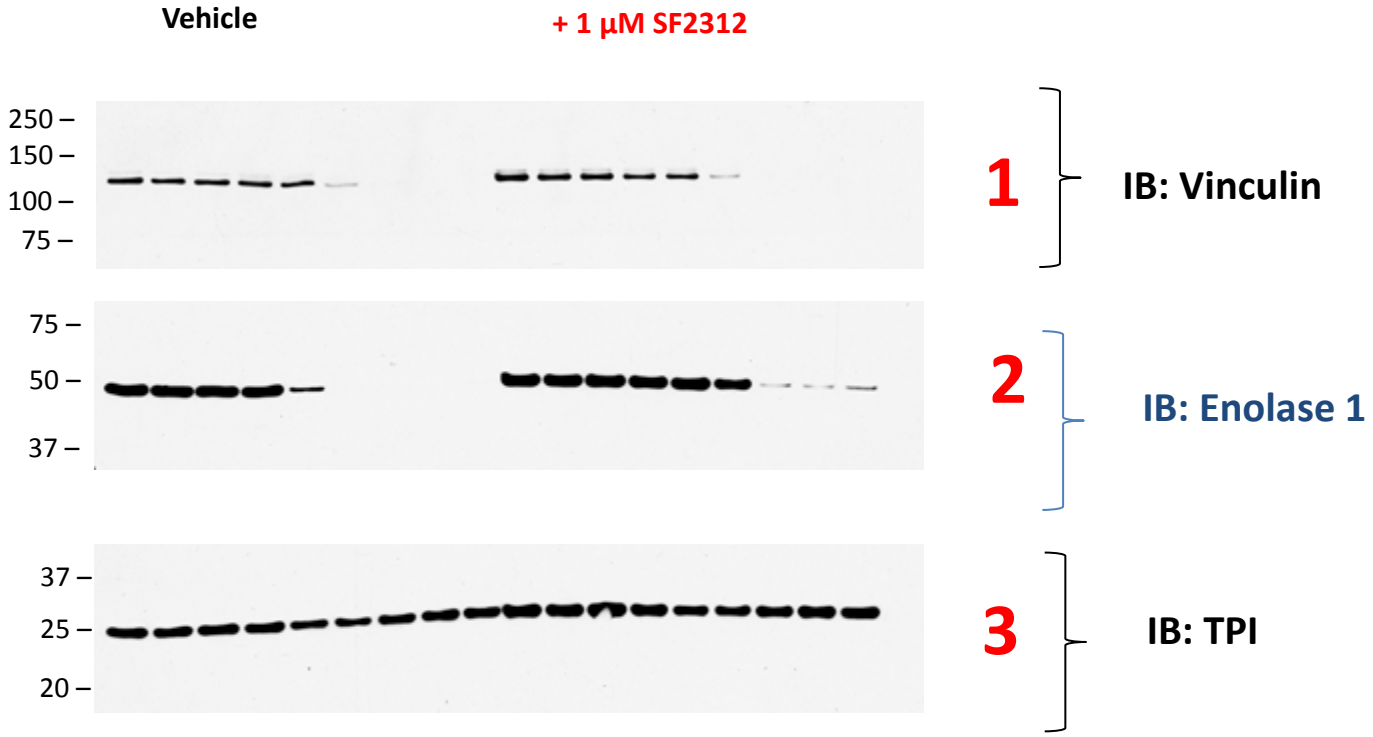

Supplementary Figure 21

B)

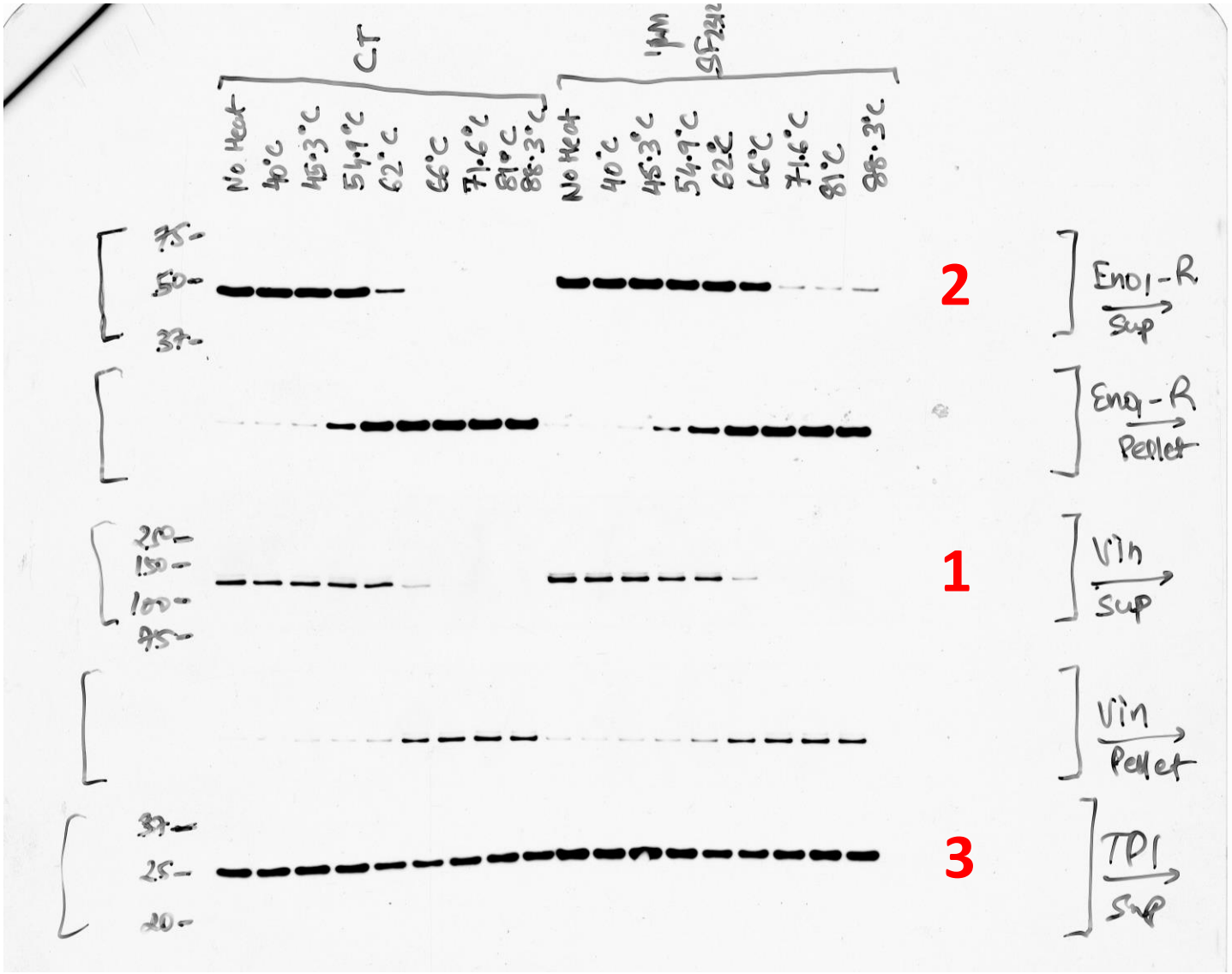

Supplementary Figure 21: *Uncropped western blot scans for Supplementary Figure 4.* **Panel A**) Partially cropped and size marker annotated western blots; **Panel B**) Raw x-ray film scans with numbers in red indicating the blots shown in figure. Lysates from thermal shift assays for Enolase 1 were size separated by electrophoresis and transferred to nitrocellulose membranes. The membranes were cut at the 75 kDa and 37 kDa size markers. The high molecular weight (250 – 75 kDa) region was blotted for Vinculin (MW = 130 kDa), while the middle (75- 37 kDa) was blotted for ENO1 (MW = 47 kDa), whilst the low molecular weight fragment was blotted for TPI (MW = 25 kDa). Numbers in red indicate which blots were used in the figures.

Supplementary Figure 22

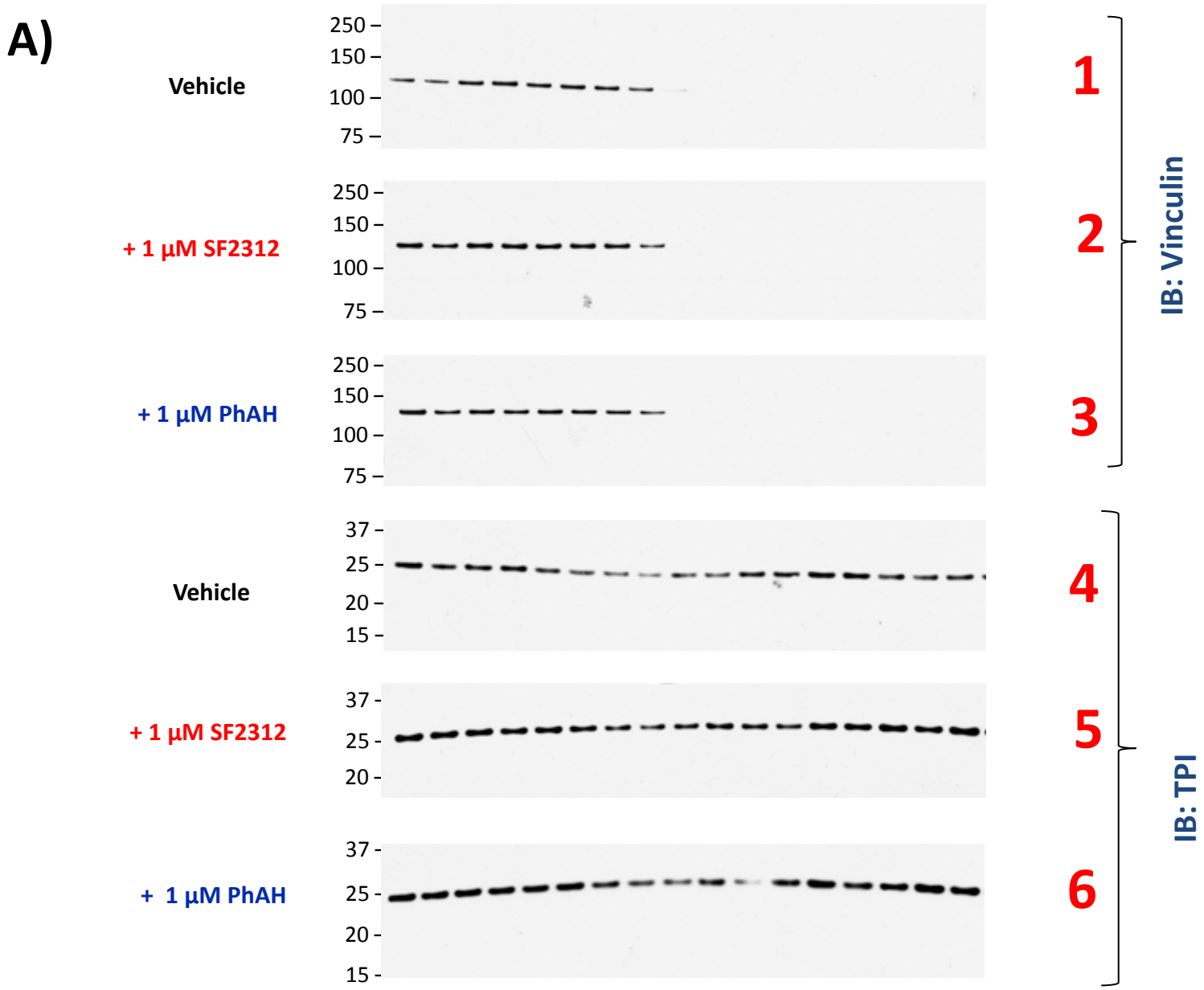

Supplementary Figure 22

B)

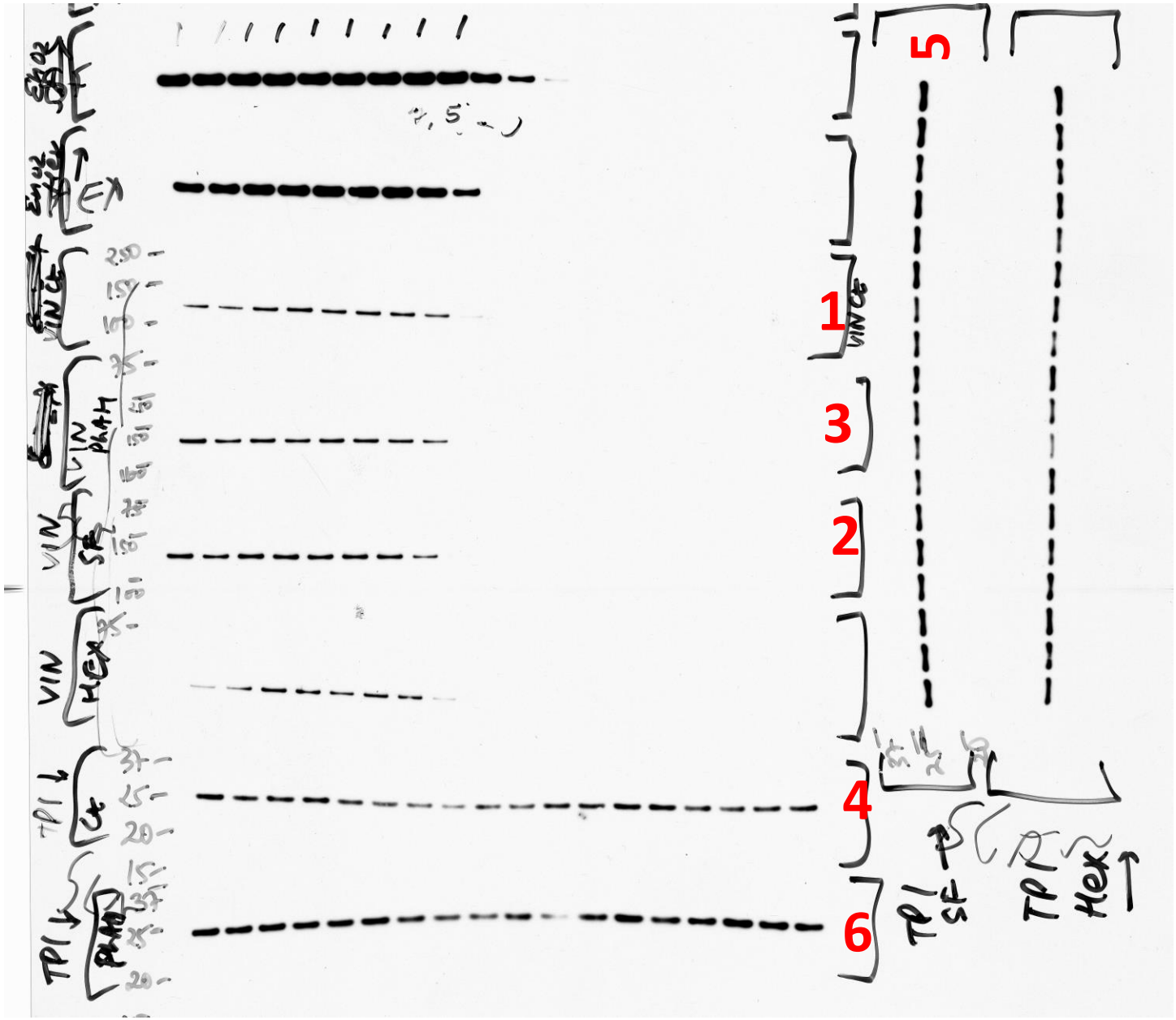

Supplementary Figure 22: *Uncropped western blot scans for Supplementary Figure 5.* **Panel A**) Partially cropped and size marker annotated western blots; **Panel B**) Raw x-ray film scans with numbers in red indicating the blots shown in figure. Lysates from thermal shift assays were size separated by electrophoresis and transferred to nitrocellulose membranes. The membranes were cut at the 75 kDA and 37 kDA size markers. The high molecular weight (250 – 75 kDa) region was blotted for Vinculin (MW = 130 kDa, while the middle (75- 37 kDa) was blotted for ENO2 (MW = 47 kDa, Supplementary Figure 20), whilst the low molecular weight fragment was blotted for TPI (MW = 25 kDa). Numbers in red indicate which blots were used in the figures.

Supplementary Figure 23

A)

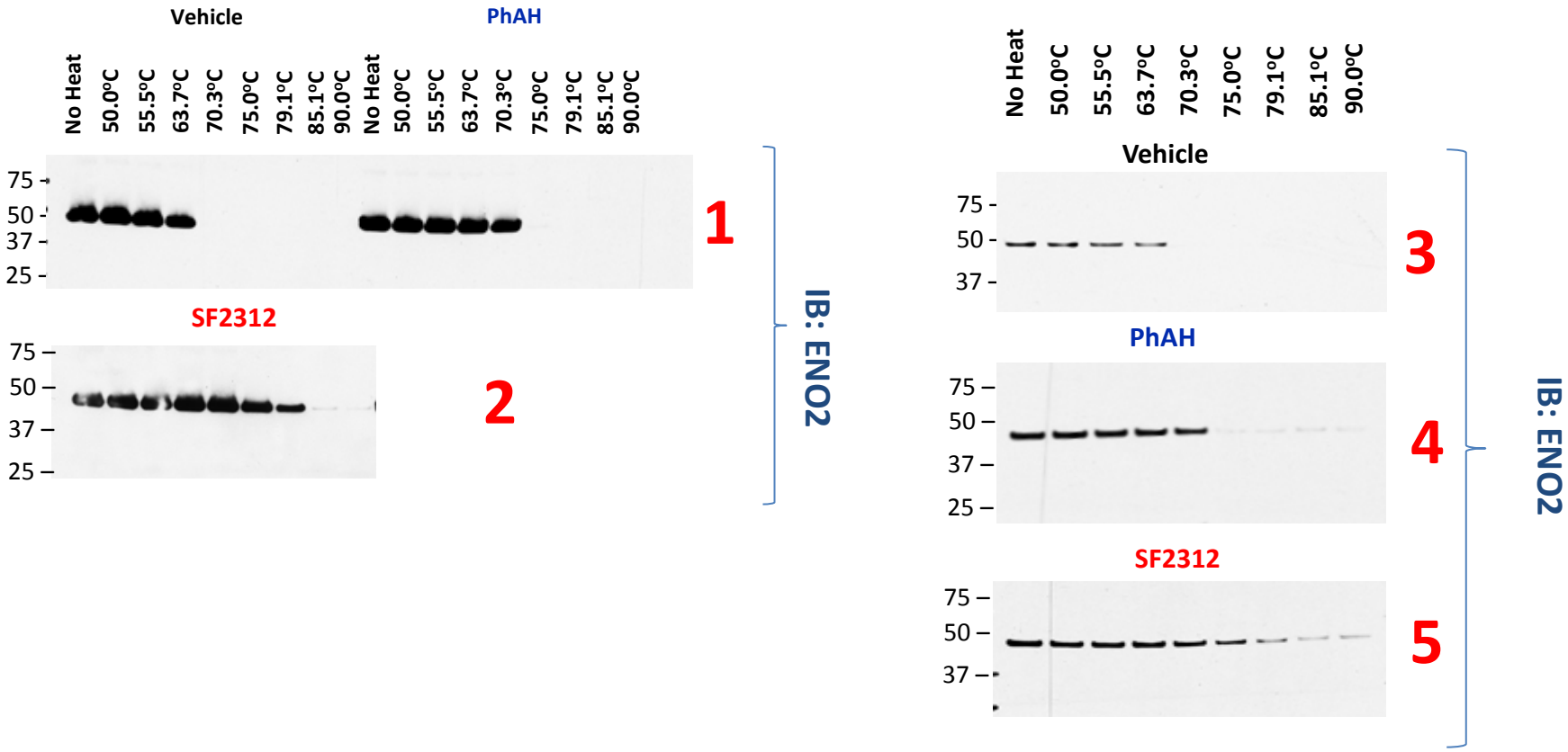

Supplementary Figure 23

B)

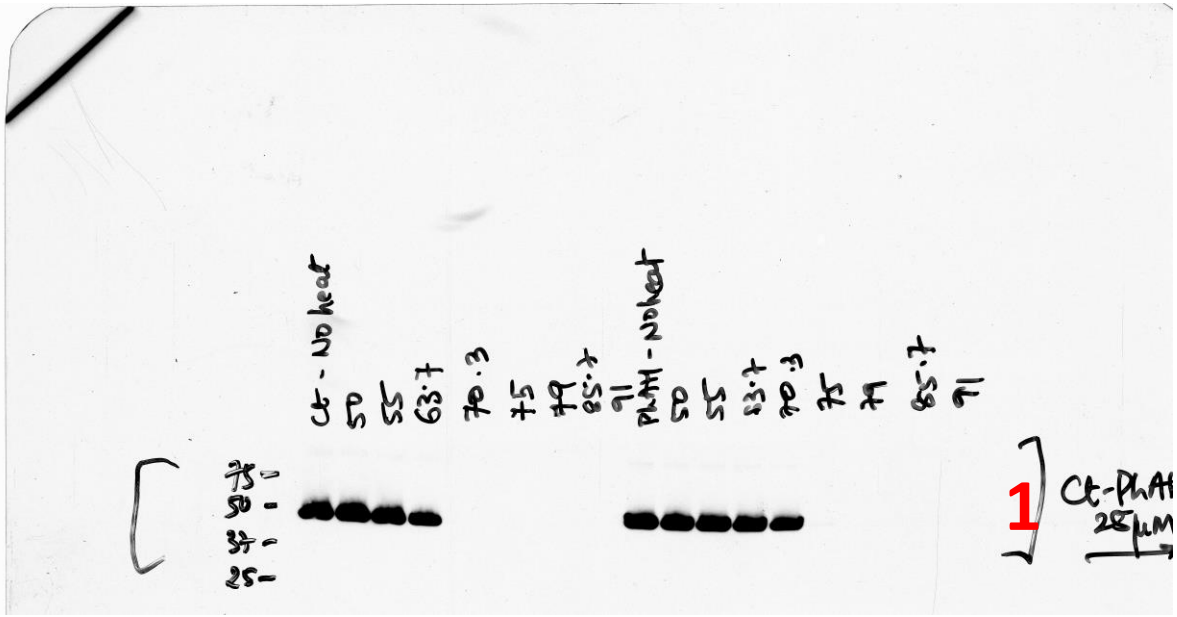

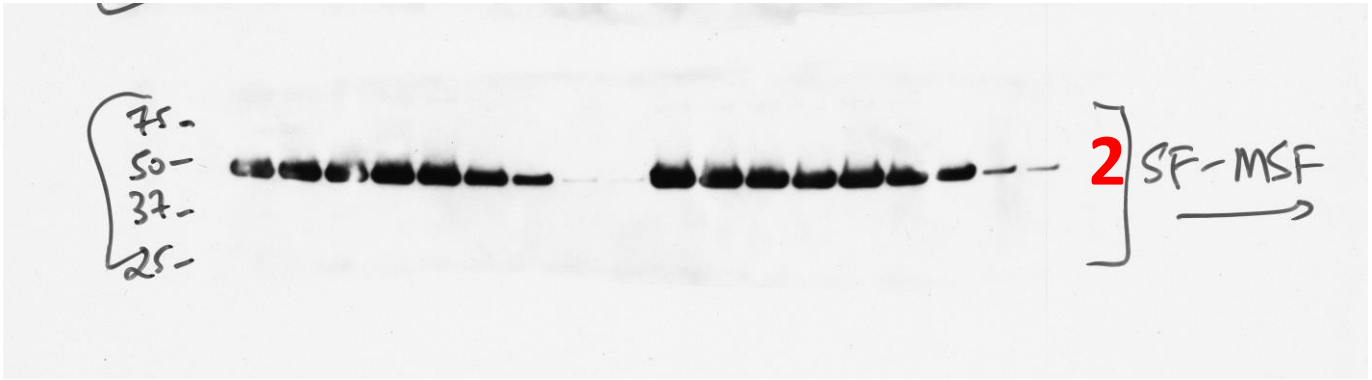

Supplementary Figure 23

B)

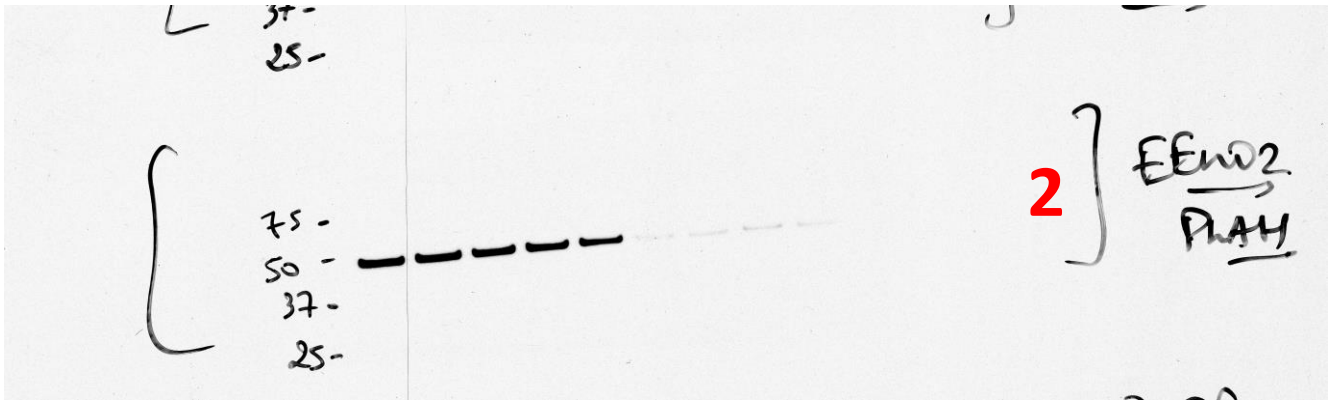

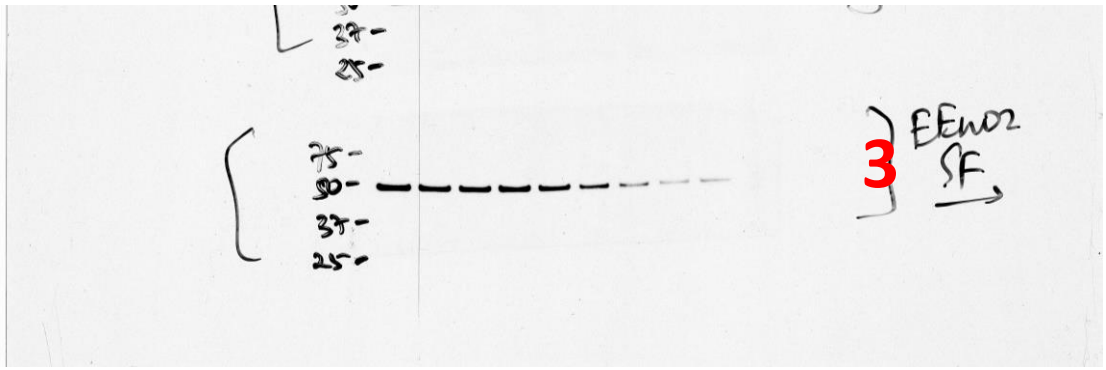

Supplementary Figure 23: *Uncropped western blot scans for Supplementary Figure 6.* **Panel A**) Partially cropped and size marker annotated western blots; **Panel B**) Raw x-ray film scans with numbers in red indicating the blots shown in figure. The membranes were cut between 75 kDa and 25 kDa and blotted against ENO2. Three thin lines are evident in the blots; they are artefactual roller streaks caused by the film developer.

Supplementary Figure 24

A)

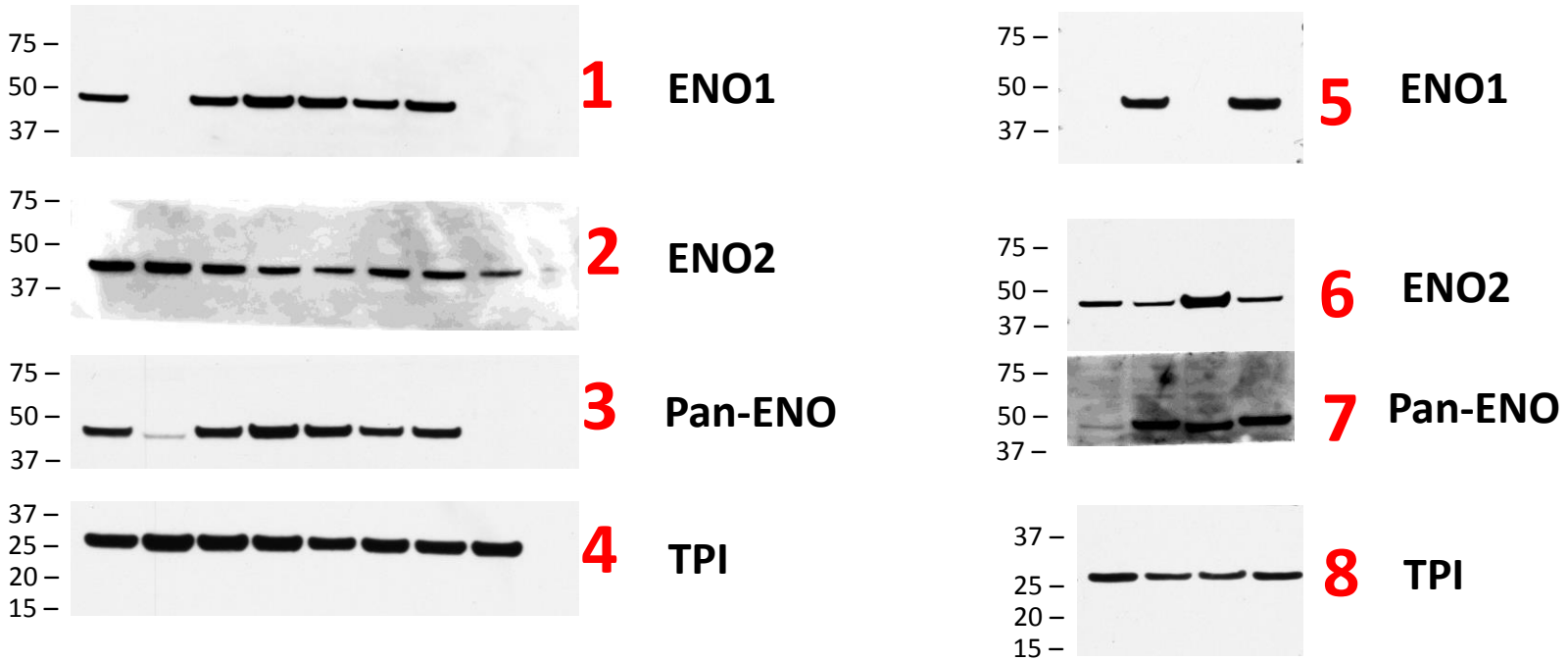

Supplementary Figure 24

B)

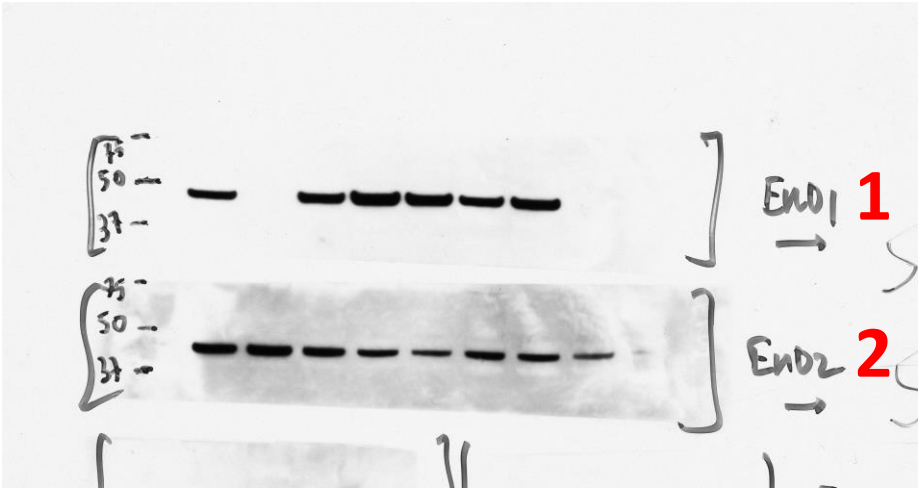

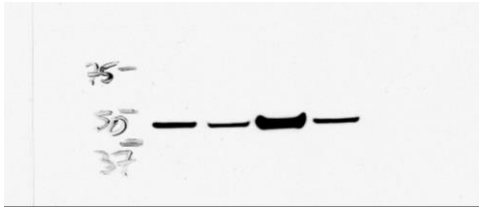

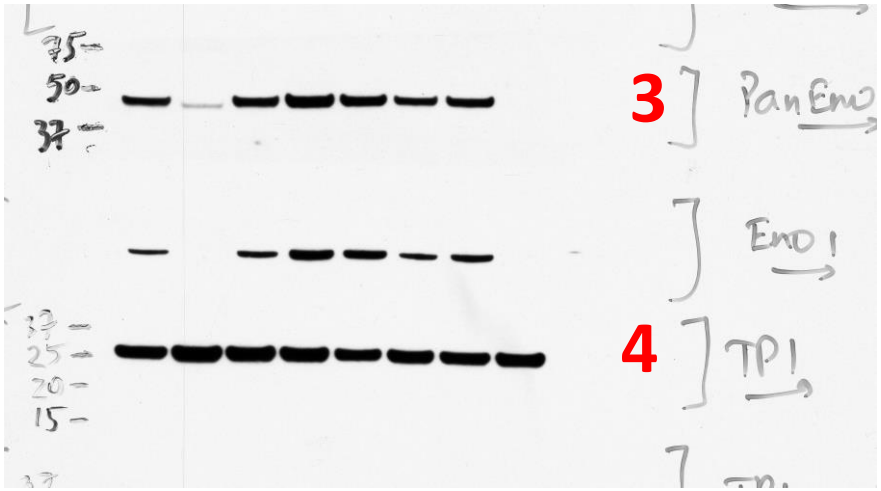

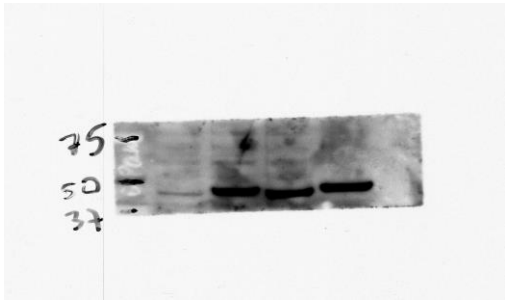

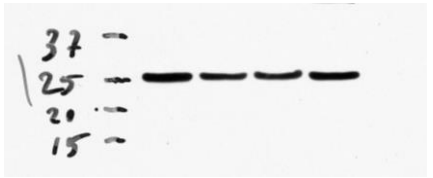

Supplementary Figure 24: *Uncropped western blot scans for Supplementary Figure 7.* **Panel A**) Partially cropped and size marker annotated western blots; **Panel B**) Raw x-ray film scans with numbers in red indicating the blots shown in figure. The membranes were cut between 75 kDa and 37 kDa and blotted against ENO1, ENO2 and Pan-Eno. The membrane lower than 37kDa was blotted against TPI. A thin line in blots 3 and 4 is a roller streak caused by the film developer.

Supplementary Figure 25

A)

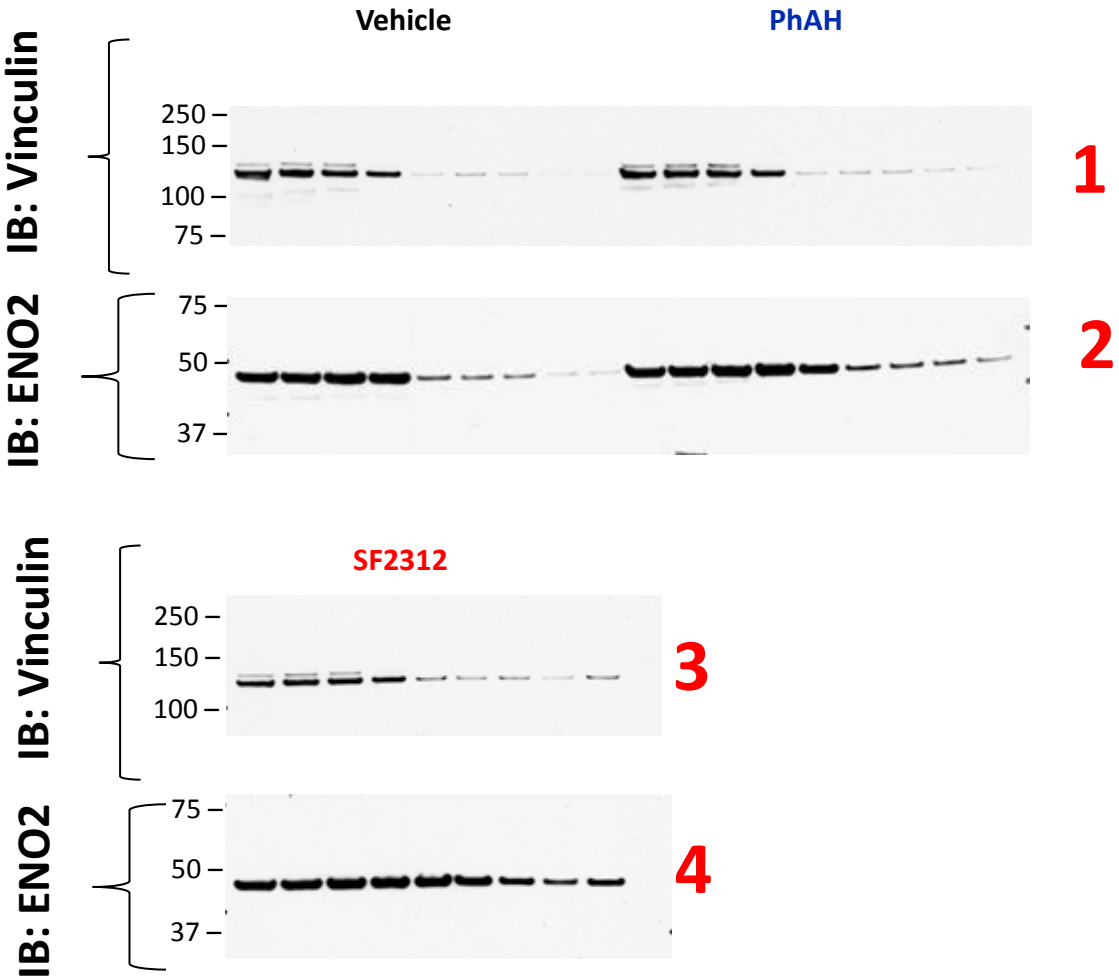

Supplementary Figure 25

B)

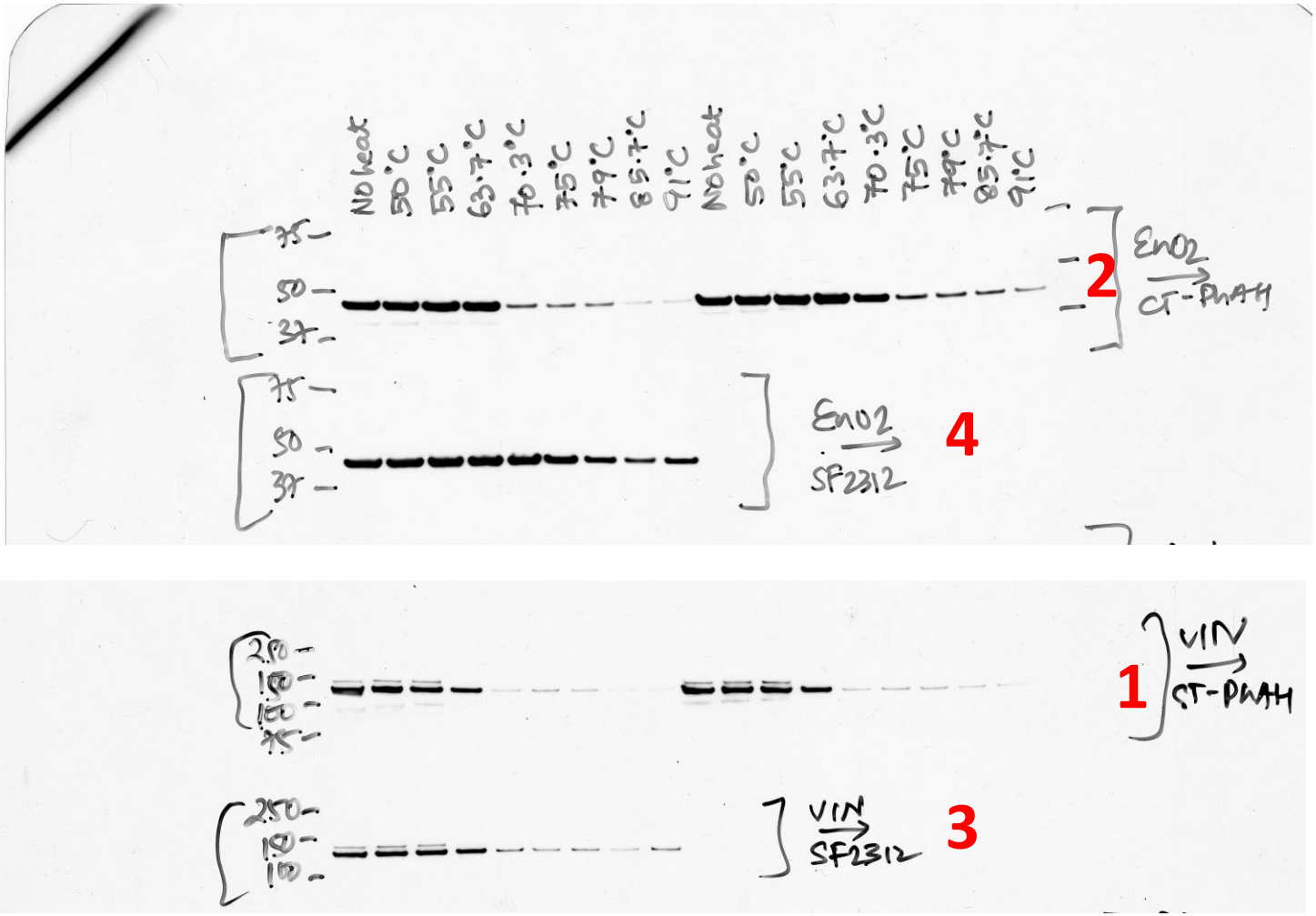

Supplementary Figure 25: *Uncropped western blot scans for Supplementary Figure 18.* **Panel A**) Partially cropped and size marker annotated western blots; **Panel B**) Raw x-ray film scans with numbers in red indicating the blots shown in figure. Lysates from thermal shift assays in intact glioma cells were size separated by electrophoresis and transferred to nitrocellulose membranes. The membranes were cut at the 75 kDA and 37 kDA size markers. The high molecular weight (250 – 75 kDa) region was blotted for Vinculin (MW = 130 kDa), while the lower (75- 37 kDa) was blotted for ENO2 (MW = 47 kDa).

Supplementary Figure 26

A)

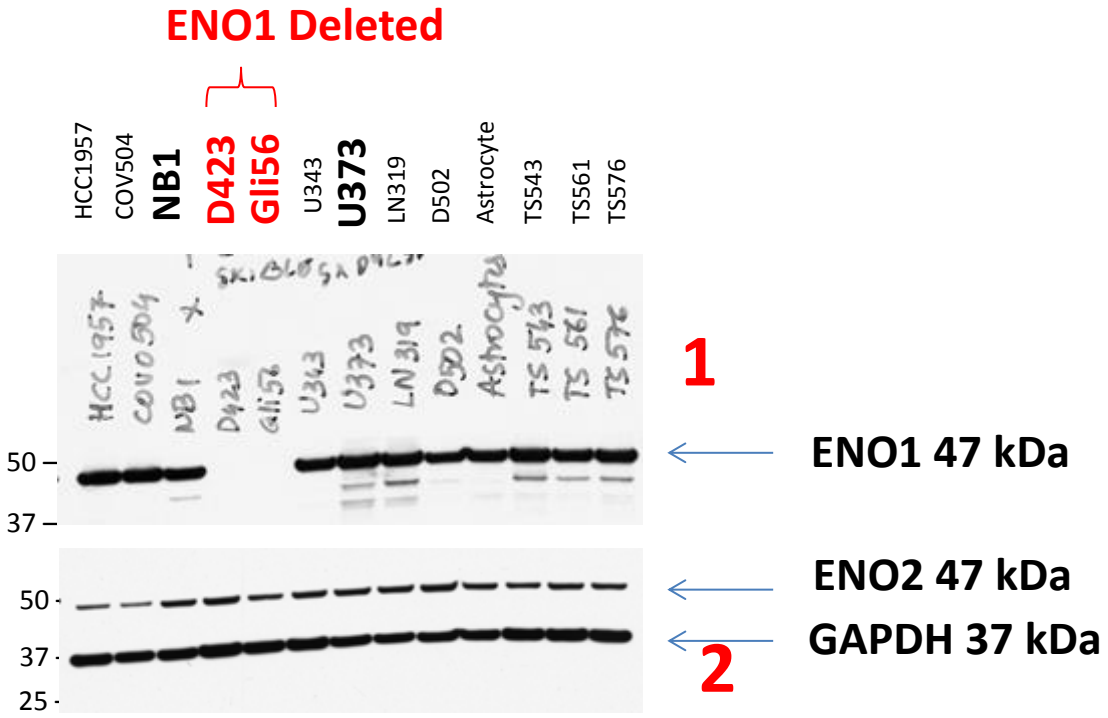

Supplementary Figure 26

B)

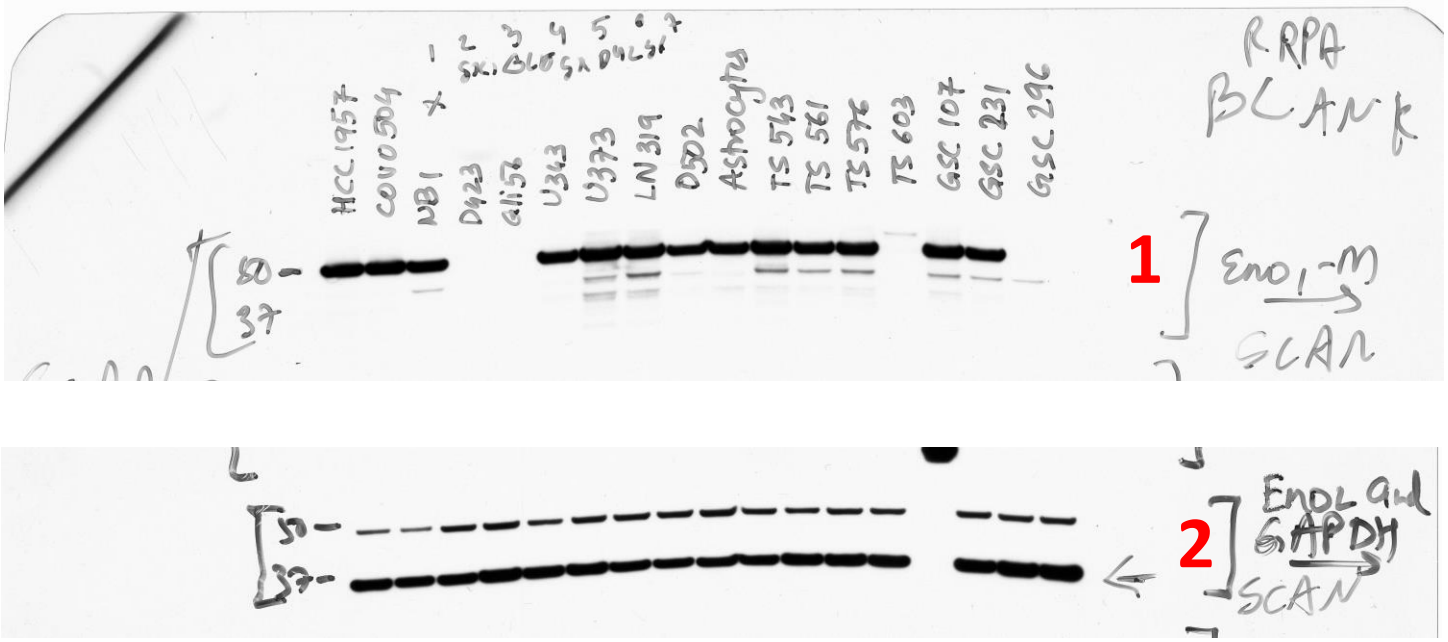

Supplementary Figure 26: *Uncropped western blot scans for Supplementary Figure 19a.* **Panel A**) Partially cropped and size marker annotated western blots; **Panel B**) Raw x-ray film scans with numbers in red indicating the blots shown in figure. The membranes were blotted for ENO1 and ENO2 (MW = 47 kDa) as well as for GAPDH (MW = 37 kDa).